Received: 28 November 2023 | Accepted: 21 August 2024

DOI: 10.1111/mice.13334

COMPUTER-AIDED CIVIL AND INFRASTRUCTURE ENGINEERING WILEY

RESEARCH ARTICLE

A convergent cross-mapping approach for unveiling congestion spatial causality in urban traffic networks

Jiannan Mao[1,2] | **Hao Huang**[3] | **Yu Gu**[4] | **Weike Lu**[5] | **Tianli Tang**[6] | **Fan Ding**[6]

[1]School of Transportation Engineering, East China Jiaotong University, Nanchang, China

[2]Department of Civil and Environmental Engineering, University of Wisconsin-Madison, Madison, Wisconsin, USA

[3]School of Transportation and Logistics, Southwest Jiaotong University, Chengdu, China

[4]Department of Civil and Environmental Engineering, The Hong Kong Polytechnic University, Hong Kong, China

[5]School of Rail Transportation, Soochow University, Soochow, China

[6]School of Transportation, Southeast University, Nanjing, China

Correspondence
Fan Ding, School of Transportation, Southeast University, Nanjing, China.
Email: fding5@seu.edu.cn

Yu Gu, Department of Civil and Environmental Engineering, The Hong Kong Polytechnic University, Kowloon, Hong Kong, China.
Email: ceeyu.gu@polyu.edu.hk

Funding information
National Natural Science Foundation of China, Grant/Award Numbers: 52102376, 62103292; Fundamental Research Funds for the Central Universities, Grant/Award Number: 2242022R40055

Abstract

Spatial causality in urban traffic networks explores how events or conditions in one location affect those in another. Unveiling congestion spatial causality is crucial for identifying congestion-inducing bottlenecks in traffic networks and offering valuable insights for traffic network management and control. This study introduces the traffic-convergent-cross-mapping (T-CCM) method, a state-space-reconstruction approach from the dynamic system perspective, to identify causality among roads within urban traffic networks using time series data. Simultaneously, it effectively addresses the intricate challenges of uncertainty and interdependency among sensors caused by traffic flow dynamics. Empirical findings from real-world (PeMS-Bay area) traffic speed data validate the effectiveness of the T-CCM method in detecting causality. This study reveals bidirectional causal effects between downstream and upstream roads in short-term congestion generation and dissipation periods, which can pinpoint congestion origins and inform quick traffic management response. Furthermore, it elucidates the long-term causality impacts between distant roads, particularly with regard to traveler choices and road land use attributes, guiding infrastructure investment and public transit improvements.

1 | INTRODUCTION

The rapid advancement of intelligent transportation systems (ITS) has facilitated the collection of time-series data from diverse sources such as sensors, roadside units, and Global Positioning System (GPS) devices. Time series data, rich in sequential observations over time, are pivotal for analyzing traffic dynamics, offering insights into traffic evolutions, patterns, and the complex interactions within urban traffic networks (G. Huang et al., 2021; Zou et al., 2024). The ability to capture the complex dynamics of traffic networks through traffic time-series data is essential

for understanding spatial dependencies and interactions among road segments.

Analyzing the spatial dependency of road sections/sensors within time-series traffic data holds great promise for both theoretical and practical applications, including traffic prediction and estimation (W. Chen et al., 2020; H. Huang et al., 2023), traffic pattern clustering (Celikoglu & Silgu, 2016; Ryu et al., 2022), traffic anomaly detection (Boquet et al., 2020), and coordinated control (Peng & Xu, 2023). By unraveling the spatial dependencies within the time-series traffic data, researchers can gain valuable insights into the underlying mechanisms that govern traffic dynamics. This understanding facilitates the development of more effective strategies for traffic management and control.

In urban traffic research, one approach to measuring spatial dependencies involves modeling traffic propagation, where the core lies in the conservation law of vehicles and the fundamental diagram. These studies can be classified into continuum models, such as Lighthill–Whitham–Richards model (Lighthill & Whitham, 1955; Richards, 1956), as well as its derivation versions that described kinematic and rarefaction waves (Jin et al., 2015; Qin et al., 2021; A. Zhou et al., 2023), and discrete models, like the cell transmission model (Jin, 2021; Z. Zhang et al., 2022), which describe traffic as a discrete process in time and space.

While these model-based methods have advanced understanding in literature, they have limitations in comprehensively describing the complexities and uncertainty inherent in urban traffic networks (Mohammadian et al., 2021; Ngoduy, 2021), often requiring adjustments for specific real-world scenarios like capacity variations(Jin et al., 2015; Kim & Cassidy, 2012), or multi-class traffic conditions (Qin et al., 2021). Achieving an accurate real-world traffic model is challenging due to noise and driver stochasticity, further complicated by the need for parameter calibration or estimation (Cheng et al., 2022; Ghosh-Dastidar & Adeli, 2006; Jiang & Adeli, 2004; Ngoduy, 2021; X. S. Zhou et al., 2022). Moreover, the literature on addressing network-wide spatial dependencies is limited, with most studies at the link or corridor level facing challenges due to the unpredictability of travel behavior and the complexity involved in accurately modeling physical dynamics across large-scale networks (Y. Chen, Mao, et al., 2022; Saeedmanesh & Geroliminis, 2016). The intricate interactions and interdependencies among various factors influencing traffic dynamics contribute to the complexity and uncertainty of the situation, making it difficult to fully capture and accurately model the underlying mechanisms. Therefore, a more general data-driven framework is preferable for real-world applications.

In addition to traditional traffic flow methods, recent research, supported by abundant traffic time-series data, has leveraged statistical mathematics and information theory methods to quantify road dependencies within urban traffic networks. Measurements such as the Pearson correlation coefficient (Habtemichael & Cetin, 2016; Ke et al., 2021) and Spearman coefficient (Dai et al., 2019) have been used to detect correlations between sensors or roads through time-series data. However, these linear measurements are inadequate for capturing the non-linear effects prevalent in complex urban traffic systems (Mohammadian et al., 2021). Moreover, it is important to acknowledge the limitations of correlation analysis when trying to capture the complex dynamics of urban traffic systems, considering the anisotropic nature of traffic propagation in the spatial-temporal domain (Daganzo, 1995). While correlations may indicate associations between variables, they do not necessarily imply a causal (cause–effect) relationship, which in traffic systems can refer to the true underlying dynamics of traffic flow that manifested as observed upstream–downstream traffic propagation patterns. That is to say, analyzing the statistical spatial causality present in time-series traffic data of roads offers a more accurate approach to infer traffic propagation and interaction between different road segments than relying on correlation analyses.

In this response, the Granger causality test has been explored to investigate spatial causality in urban traffic networks (L. Li et al., 2015; K. Zhang et al., 2020). Granger causality framework (Granger, 1969) is proposed based on the assumption that if a variable x has unique information that can improve the prediction of variable y, then x can be regarded as the causal of y. However, it should be noted that the Granger causality test may not be well-suited for identifying causality in urban traffic systems. The challenge arises from the requirement of independent variables as a prerequisite in the Granger causality test (Granger, 1969; Sugihara et al., 2012), while characterizing participants of the urban traffic system as independent from one another is inappropriate due to traffic propagation. In urban networks, each pair of upstream and downstream time series may contain information from each other, namely, interdependency between sensors caused by traffic flow dynamics. This renders the Granger causality test less suitable for non-separable urban traffic systems.

Given the limitation of Granger causality tests in identifying spatial causality in urban traffic networks, an alternative approach is required to overcome the challenges posed by the interdependency and system uncertainty inherent in such complex systems. Fortunately, state-space reconstruction (or attractor reconstruction) from time-series data presents a promising solution for analyzing the non-separable dynamic system (Perretti et al., 2013; Ye, Beamish, et al., 2015). Based on Takens' embedding theorem (Takens, 1981), this method enables the reconstruction

of the state space of a dynamical system from its observed time-series data, which essentially embeds the data into a higher-dimensional space. Consequently, this process reveals hidden patterns of interaction relationships within the dynamical system that are not evident in the observed or provided time-series (Ge & Lin, 2022). State-space reconstruction method has played an important role in analyzing non-linear dynamic systems across various fields, including economics, ecology, and information systems (Deyle et al., 2016; Leng et al., 2020; Perretti et al., 2013; Runge, 2018; Wang et al., 2020). Specifically, Sugihara et al. (2012) introduced a theoretical method known as convergent cross-mapping based on state-space reconstruction, which aims to detect statistical causality in dynamic systems. This method bridges the gaps left by the Granger causality tests, particularly in detecting causal relationships in non-separable systems.

This paper aims to address the challenges of uncertainty and road interdependency in detecting the spatial dependency, especially spatial causality, of urban traffic systems. Inspired by the work of Sugihara et al. (2012), we propose a spatial causality detection framework for dynamic traffic systems, named traffic convergent cross-mapping (T-CCM). The T-CCM method aims to uncover the spatial causality among road segments using only traffic time-series data collected from sensors. Based on the reconstructed road state system from time-series data, it identifies both short-term causal impacts observed through nearby sensors during congestion periods and long-term causal impacts influenced by factors at monthly or even yearly scales, such as vehicle travel preferences, land usage, and points of interest (POIs). Specifically, this method offers insights into traffic propagation across roads at various temporal scales, aiding in the identification of roads or clusters requiring targeted intervention to mitigate or prevent congestion. This contributes to improved traffic flow and enhanced urban mobility. Summing up, the main contributions of this work are as follows:

1. This study presents T-CCM, a novel causality detection method designed for urban traffic networks, which employs state-space analysis. Different from traditional traffic-flow-based approaches, T-CCM identifies network traffic interactions between sensors, offering new avenues to interpret traffic evolution in dynamic urban systems.
2. By employing only traffic time-series data, T-CCM overcomes the challenges of sensor interdependency and inherent uncertainty within urban traffic networks when assessing spatial dependencies among roads. This approach enables a clear and precise evaluation of spatial causality, thereby improving the analysis of urban traffic dynamics.
3. The T-CCM method offers a dual time-scale analysis, capturing both the immediate, short-term road interactions and the broader, long-term trends within urban traffic networks. With different time-series input lengths, T-CCM can depict short-term congestion propagation between sensors as well as long-term behaviors, such as spatial aggregation and travel choices, which are crucial for effective traffic management and planning.

Compared with recent studies on identifying relationships among roads, such as spatial dependency correlation measurement (Ke et al., 2021) and the Granger causality method (L. Li et al., 2015), the T-CCM method can measure causality among roads within urban traffic networks, considering system uncertainty and road interdependency, as detailed in Table 1.

The rest of this paper is organized as follows. Section 2 introduces the basic definition and mathematical theories of state-space reconstruction and T-CCM. Section 3 illustrates the experiment results and analyses of the T-CCM method based on real-world data. This section also presents discussions and limitations. Finally, conclusions and potential future works are summarized in Section 4.

2 | METHODS

This section outlines the mathematical method, starting with the introduction of state-space reconstruction for traffic systems, followed by the elaboration of the T-CCM method designed for spatial causality detection in urban traffic networks.

2.1 | State-space reconstruction for traffic systems

As a dynamic system evolving over time, the trajectory paths depicting the interactions between its components converge to a mathematical construct called a "manifold" denoted as $\mathbf{M}$ (Perretti et al., 2013; Ye, Beamish, et al., 2015). The manifold is introduced as a geometric representation to capture the underlying dynamics of the system, where each point represents a unique state of the system. However, directly accessing the manifold can be challenging, mainly due to its high dimensionality and complexity in real-world systems.

To overcome this challenge, a technique known as state-space (or attractor) reconstruction has been proposed to approximately estimate the origin manifold. This approach suggests that if a set of time series from a single variable belongs to a manifold $\mathbf{M}$, then its corresponding shadow manifold, denoted as $\mathbf{M}_s$, can be reconstructed through

TABLE 1 Method comparison.

Methods	Identified relationships	System uncertainty	Road interdependency
Spatial correlation	Correlation	×	–
Granger causality	Causality	–	×
T-CCM (this paper)	Causality	√	√

Abbreviation: T-CCM, traffic-convergent-cross-mapping.

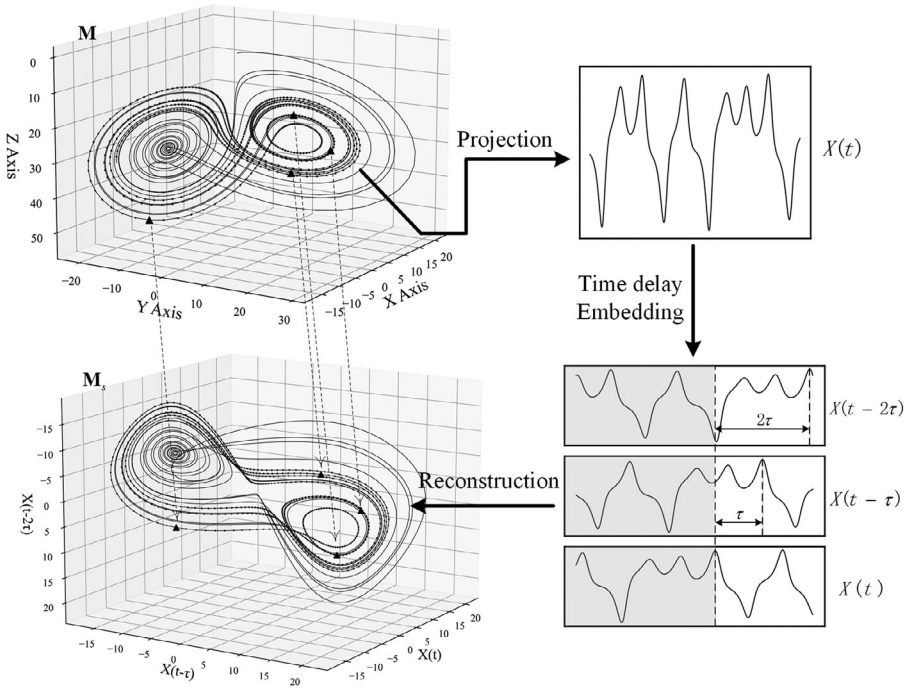

FIGURE 1 State-space reconstruction illustration, Lorenz System (Uzal et al., 2011).

a lagged-coordinate embedding operation (Takens, 1981). This reconstructed shadow manifold is a representation of the system's dynamics based on limited observations. The state-space reconstruction process to construct the shadow manifold $\mathbf{M}_s$ for time t proceeds as follows:

$$\mathbf{M}_s = [S(t), S(t-\tau), \ldots, S(t-(E-1)\tau)] \quad (1)$$

where $S(\cdot)$ denotes the system's observation vector, representing a series of dynamical projections on a certain coordinate axis; t is the time index; τ is the positive time lag; E is the embedding dimension (ranging between d and 2d + 1, where d is the dimension of the system (Deyle et al., 2016; Takens, 1981)). The parameter τ determines the time interval between successive data points used for embedding, while E determines the dimension of the reconstructed state space. Thus, the shadow manifold $\mathbf{M}_s$ can be approximately reconstructed through vectors.

To illustrate the state-space reconstruction of dynamic systems, we consider the well-known Lorenz System with classical values of parameters (Kuznetsov et al., 2020) shown in Figure 1. The upper-left shows the real manifold $\mathbf{M}$ depicted through trajectories in three-dimensional (X-Y-Z) space. The projection of the real manifold on the X-axis generates a one-dimensional time-series $X(t)$. Next, the time-delay embedding process is employed by taking $X(t)$ as the original time-series and time lagged unit τ, generating two time-series $X(t-\tau)$ and $X(t-2\tau)$ for reconstruction.

Given these three time series as new coordinates of the reconstructed space, the shadow manifold $\mathbf{M}_s$ can be rebuilt as shown in the left-bottom plot of Figure 1. The shadow manifold exhibits geometric structures and local properties similar to those of the original manifold $\mathbf{M}$. For instance, certain properties of the space at same-time points, denoted by triangles, remain unchanged, preserving the relationships between points and the overall shape of the attractor. This is attributed to the topologically invariant of the two manifolds ($\mathbf{M}_s$ and $\mathbf{M}$; Takens, 1981; Wang et al., 2020), thereby allowing to study the dynamics of $\mathbf{M}$ through its accessible representation $\mathbf{M}_s$ based on available time-series data. This process exemplifies how

to reconstruct a state space from time series data, a foundational step in the T-CCM method for analyzing urban traffic networks.

Urban traffic networks can be regarded as dynamic systems where roads, vehicles, and traffic signals interact in complex ways. The challenge in urban traffic systems, similar to understanding the Lorenz System's chaos, lies in capturing the complete state-space of the system's manifold. This is often impractical due to the limitations in measurement capabilities and the discrete nature of traffic data collection. Yet, by employing state-space reconstruction techniques, the traffic process ϕ can be reconstructed to shadow manifold $\mathbf{M}_s$ by time-series data representing fundamental traffic variables such as speed.

In this context, our study focuses on traffic speed as the primary observational variable for the urban traffic system, while acknowledging that volume or occupancy could alternatively be used. For a set of roads $\mathbf{r} = \{r_1, r_2, \dots, r_N\}$, each road/sensor is treated as a unique subsystem of the network, leading to the creation of a set of road shadow manifolds $\mathbf{M}_S^{\mathbf{r}} = \{\mathbf{M}_S^{r_1}, \mathbf{M}_S^{r_2}, \dots, \mathbf{M}_S^{r_n}\}$, each approximating the system's dynamics within the constraints of data availability. Specifically, the shadow manifold for each subsystem (road) is approximately formulated as

$$\mathbf{M}_S^{r_i} = \left[\mathbf{S}_t^{r_i}, \mathbf{S}_{t-\tau}^{r_i}, \dots, \mathbf{S}_{t-(E-1)\tau}^{r_i}\right] \tag{2}$$

where $\mathbf{S}_{t-(E-1)\tau}^{r_i}$ represents the traffic speed vector of road r_i at time $t-(E-1)\tau$, where $1+(E-1)\tau \le t \le T$, and T is the total time-series length.

The state-space reconstruction approach, as described above, serves as a foundational tool for subsequent analysis. One of the primary strengths of this approach is its ability to approximate the underlying dynamic system using a single type of time-series data. This is particularly beneficial for urban traffic systems, where fully capturing the underlying manifold of the system is often impractical.

2.2 | T-CCM for urban traffic causality detection

2.2.1 | Preliminaries and overall framework

It is widely acknowledged that participants within urban traffic systems exhibit interactions and correlations with each other. Beyond these correlations, there also exist causal relationships between participants. The T-CCM approach is introduced to tackle challenges in detecting spatial causality within traffic time-series data, specifically adapted to handle the uncertainty and interdependency encountered in analyzing urban traffic dynamics.

The T-CCM method for detecting spatial causality in urban traffic systems can be formulated as follows: Given the network-scale time-series data of traffic speed $\mathbf{S}_{\mathbf{t}}^{\mathbf{r}} \in \mathbb{R}^{T\times N}$, where $\mathbf{r} = \{r_1, r_2, \dots, r_N\}$ represents a set of roads and $\mathbf{t} = \{t_1, t_2, \dots, t_T\}$ is the set of time stamps, calculate the causality matrix $\mathbf{C}_{NN} \in \mathbb{R}^{N\times N}$ that reflects the strength of causal interactions between roads with different input lengths.

Figure 2 illustrates the framework of the T-CCM method for uncovering spatial causality in traffic speeds across an urban network with the following steps:

Step 1: Initialize with a speed matrix for N roads over time T, considering each road as a subsystem. Conduct state-space reconstruction using embedding dimension (E), delay time (τ), and the number of time lags (L, $L = T-(E-1)\tau$), and obtain a traffic speed state space for each road/sensor as a $L \times E$ matrix.

Step 2: Identify the $E+1$ nearest neighbors and their time indices for each speed state vector in the reconstructed speed state space of each road. For each road, there will be $L \times (E+1)$ format.

Step 3: Calculate normalized distance weights for each speed vector, reflecting the relative proximity of vector points. These weights form a weight distance matrix and will be used to estimate the shadow manifold for each road.

Step 4: Quantify the causality coefficient for road pairs by comparing the differences between the estimated and original reconstructed speed shadow manifolds, encapsulated in the causality matrix.

Specifically, if the state of one road causally influences another, this interaction is captured within the shadow manifolds: The state information of the influencing road is recorded within the shadow manifold of the influenced road. Moreover, the strength of this causal relationship is quantifiable by assessing the convergence between the estimated shadow manifold of the influencing road—derived from the shadow manifold of the influenced road—and the actual shadow manifold of the influencing road itself. This is also the core of the causality coefficient matrix calculation process, wherein the elements, causality coefficient values, are computed by quantifying the differences between the actual values in the shadow manifold and their respective estimations.

2.2.2 | Causality coefficient matrix calculation

Given the spatial-temporal speed data $\mathbf{S}_{\mathbf{t}}^{\mathbf{r}}$ with the shape of (T, N), where T denotes the total time stamps and N represents the number of roads, the state-space reconstruction, with the embedding dimension E and the time delay lag τ,

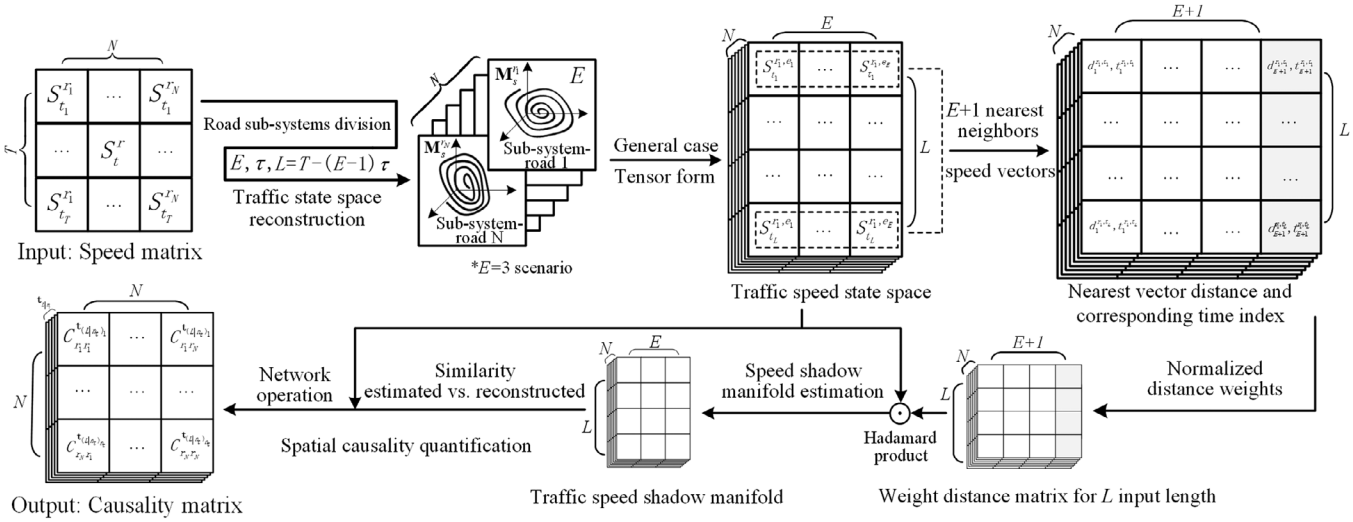

FIGURE 2 Overall framework of traffic-convergent-cross-mapping (T-CCM).

generates the speed shadow manifold for road r_i as a subsystem can be $M_s^{r_i,T-(E-1)\tau,E} = \left[\mathbf{S}_t^{r_i,E}, \mathbf{S}_{t-\tau}^{r_i,E}, \ldots, \mathbf{S}_{t-(E-1)\tau}^{r_i,E}\right] \in \mathbb{R}^{(T-(E-1)\tau)\times E}$. For simplicity, we set the input time length as $L = T-(E-1)\tau$ and the time stamp set as $\mathbf{t}_{\mathrm{L}} = \{t_1, t_2, \ldots, t_L\}$. Consequently, a three-dimensional tensor $[\mathbf{M}_s]_{N\times L\times E} = \{\mathbf{M}_s^{r_1,L,E}, \mathbf{M}_s^{r_2,L,E}, \ldots, \mathbf{M}_s^{r_N,L,E}\}$ with the shape of (N, L, E) is formed to represent the network's speed shadow manifold.

For each road r_i in the network, the first step is to find the $E+1$ nearest neighbors of vectors in the speed shadow manifold for each time stamp t ($t \in \mathbf{t}_{\mathrm{L}}$). The distance between vectors at time stamps can be calculated using Equation (3), where $d_{t_at_b}^{r_i}$ is the E-dimensional Euclidean distance between time stamps t_a and t_b in the shadow manifold $\mathbf{M}_s^{r_i,L,E}$ of road r_i; $S_{t_a}^{r_i,e_j}$ and $S_{t_b}^{r_i,e_j}$ denote the element of the jth dimension on time stamp t_a and t_b, respectively.

$$d_{t_at_b}^{r_i} = \left(\sum_{e_j=1}^{E}\left(S_{t_a}^{r_i,e_j} - S_{t_b}^{r_i,e_j}\right)^2\right)^{1/2} \tag{3}$$

Subsequently, for each time stamp t, the distances of $E+1$ nearest neighbors of vectors, along with their corresponding time indices, are restored in descending order using Equations (4) and (5):

$$\mathbf{D}_{E+1}^{r_i,t} = \left[d_1^{r_i,t}, d_2^{r_i,t}, \ldots, d_{E+1}^{r_i,t}\right] \tag{4}$$

$$\mathbf{t}_{E+1}^{r_i,t} = \left[t_1^{r_i,t}, t_2^{r_i,t}, \ldots, t_{E+1}^{r_i,t}\right] \tag{5}$$

where $\mathbf{D}_{E+1}^{r_i}$ and $\mathbf{t}^{r_i,t}$ are the distance vector, ordered by closeness of $E+1$ nearest neighbors of vectors, and its corresponding time index vector at time stamp t, respectively; $d_p^{r_i,t}$ and $t_p^{r_i,t}$ denote the distance and its corresponding time index of the pth nearest point of the speed vector at time t, respectively.

Extending this to the input time length L, the recorded distance forms a matrix with the shape of $(L, E+1)$, denoted as $\mathbf{D}_{E+1}^{r_i,\mathbf{t}_L} = [\mathbf{D}_{E+1}^{r_i,t_1}, \mathbf{D}_{E+1}^{r_i,t_2}, \ldots, \mathbf{D}_{E+1}^{r_i,t_L}]^{\mathrm{T}} \in \mathbb{R}^{L\times(E+1)}$. Analogously, the corresponding time index matrix can be $\mathbf{t}_{E+1}^{r_i,\mathbf{t}_L} = [\mathbf{t}_{E+1}^{r_i,t_1}, \mathbf{t}_{E+1}^{r_i,t_2}, \ldots, \mathbf{t}_{E+1}^{r_i,t_L}]^{\mathrm{T}} \in \mathbb{R}^{L\times(E+1)}$. Note that according to Equations (2) and (3), the input time length should fall within the range of $(E+1, T-(E-1)\tau)$.

Next, the normalized distance weight, used for speed shadow manifold estimation, can be calculated as Equations (6)–(8):

$$\mathbf{u}_{E+1}^{r_i,t_j} = \exp\left(-\mathbf{D}_{E+1}^{r_i,t_j}/\mathbf{D}_{E+1}^{r_i,t_1}\right) \tag{6}$$

$$\mathbf{w}_{E+1}^{r_i,t_j} = \mathbf{u}_{E+1}^{r_i,t_j}/\sum_{e=1}^{E+1}\mathbf{u}_e^{r_i,t_j} \tag{7}$$

$$\mathbf{w}_{E+1}^{r_i,\mathbf{t}_L} = \left\{\mathbf{w}_{E+1}^{r_i,t_1}, \mathbf{w}_{E+1}^{r_i,t_2}, \ldots, \mathbf{w}_{E+1}^{r_i,t_L}\right\} \in \mathbb{R}^{L\times(E+1)} \tag{8}$$

where $\mathbf{u}_{E+1}^{r_i,t_j}$ is the Euclidean distance weight for road r_i at time t_j ($t_j \in \mathbf{t}_L$), with the shape of $(1, E+1)$; $\mathbf{w}_{E+1}^{r_i,t_j}$ denotes the normalized distance weight of r_i, which is obtained by dividing $\mathbf{u}_{E+1}^{r_i,t_j}$ by its summation of the Euclidean distance weight along $E+1$ vectors; $\mathbf{w}_{E+1}^{r_i,\mathbf{t}_L}$ represents the normalized weight matrix for the input time length L.

The speed shadow manifold estimation process can now be carried out using the time index matrix $\mathbf{t}_{E+1}^{r_i,L}$ and normalized weight matrix $\mathbf{w}_{E+1}^{r_i,\mathbf{t}_L}$. Considering an arbitrary pair of roads r_X and r_Y, with road r_Y being the target one. The

estimation of shadow manifold of r_Y can be calculated as

$$\hat{Y}(L)|\mathbf{M}_s^{r_X} = \sum_{e=1}^{E+1} \mathbf{w}_e^{r_X,\mathbf{t}_L} \odot \mathbf{M}_s^{r_Y,\mathbf{t}_{E+1}^{r_X,L},e} \tag{9}$$

where $\hat{Y}(L)|\mathbf{M}_s^{r_X}$ represents the estimated speed shadow manifold of road r_Y based on the shadow manifold of r_X, with the input time length L; $\mathbf{w}_e^{r_X,\mathbf{t}_L}$ denotes the normalized weight matrix of the eth dimension, generated from the shadow manifold of r_X, and the symbol $\odot$ denotes the Hadamard product; $\mathbf{M}_s^{r_Y,\mathbf{t}_{E+1}^{r_X,L},e}$ is obtained from the shadow manifold of r_Y, where the vectors of the second dimension are assigned by the time index matrix $\mathbf{t}_{E+1}^{r_X,\mathbf{t}_L}$ of r_X.

Consequently, the causality coefficient of r_Y affected by r_X with input time series set $\mathbf{t}_L$, $C_{r_X r_Y}^{\mathbf{t}_L}$, can be computed through Equation (10) as follows:

$$C_{r_X r_Y}^{t_L} = \bar{\rho}\% \left(\mathbf{M}_s^{r_Y,L,E}, \hat{Y}(L)\middle|\mathbf{M}_s^{r_X}\right) \tag{10}$$

where $\bar{\rho}$ denotes the mean calculation process of the correlation coefficient (correlation calculation in this paper, ranging from −1 to 1), aiming at measuring how well the estimation values couple to the real values; $\mathbf{M}_s^{r_Y,L,E}$ is the reconstructed shadow manifold of r_Y, and $\hat{Y}(L)|\mathbf{M}_s^{r_X}$ represents the estimated shadow manifold of road r_Y based on the shadow manifold of r_X. For the whole network, Equation (10) can be converted to the matrix form as $\mathbf{C}_{NN}^{\mathbf{t}_L} \in \mathbb{R}^{N\times N}$, indicating the causality coefficient between each pair of roads, which can be treated as a quantification of causal relationships.

Furthermore, the necessary condition for causality between two roads is that the causality coefficient values converge to a higher value with an increase in input time-series length. As the length of time-series data goes longer, the reconstructed shadow manifold will become denser, resulting in more accurate recorded information. Therefore, it is essential to evaluate the convergence of the causality coefficient by incrementally increasing the input length. Let n_t denotes the number of chosen input lengths, and the step size for increasing the input length can be set as dividing L by n_t, denoted as $L|n_t$. Then the lth input length can be $[L|n_t]_l$. It should be noted that the choice of n_t depends on specific needs, and a larger value will create a smoother result. Consequently, the input time length set can be defined as $\mathbf{t}_{L|n_t} = \{\mathbf{t}_{(L|n_t)_1}, \ldots, \mathbf{t}_{(L|n_t)_l}, \ldots, \mathbf{t}_L\}$, where $\mathbf{t}_{(L|n_t)_l} = \{t_1, t_2, \ldots, t_{[L|n_t]_l}\}$. The causality coefficient matrix $\mathbf{C}_{NN}^{\mathbf{t}_{L|n_t}} = \{\mathbf{C}_{NN}^{\mathbf{t}_{(L|n_t)_1}}, \ldots, \mathbf{C}_{NN}^{\mathbf{t}_{(L|n_t)_l}}, \ldots, \mathbf{C}_{NN}^{\mathbf{t}_L}\}$ can be calculated with this input time length set.

In conclusion, the T-CCM method, by analyzing traffic time-series data from each road/sensor, enables the reconstruction of speed shadow manifolds and the computation of the causality coefficient matrix, revealing causal relationships between road segments. Its versatility in managing the complexities of urban traffic systems and easy application in various settings, using basic time-series data with minimal limitations, marks T-CCM as an invaluable approach. Adjusting input lengths improves insight into the underlying dynamics of traffic interactions and patterns across various time scales, showcasing its significant influence on urban traffic network analysis.

3 | EXPERIMENTS AND ANALYSES

In this section, we begin by assessing the effectiveness of the proposed T-CCM method using real-world network traffic speed data with varying input time lengths. Subsequently, the evaluation of short-term traffic propagation between upstream and downstream sensors during congestion generation and dissipation periods is conducted by examining spatial causality using the T-CCM approach. Additionally, network analysis is established to investigate the long-term traffic interactions within a causality framework, using input lengths of approximately a month to capture the comprehensive temporal and spatial effects of traffic propagation. Toward the conclusion of this section, we address the limitations of our work and discuss potential avenues for future enhancements.

3.1 | Test base and settings

The traffic speed data utilized in this study, derived from the California Department of Urban Traffic (Caltrans) Performance Measurement System (PeMS, http://pems.dot.ca.gov), specifically focuses on the PeMS-Bay data, a benchmark previously explored in the former study (Y. Li et al., 2017). This dataset comprises traffic speed data from 318 sensors over 5 months (January 1, 2017, to May 31, 2017), generating 52,117 data points with traffic speeds recorded every 5 min. Despite its collection in 2017, the PeMS-Bay dataset continues to stand as a pivotal benchmark in recent traffic research, particularly in the traffic prediction domain. Figure 3 displays the location of sensors for visualization purposes. Additionally, to provide visual insights into the T-CCM algorithm's outcomes under different landscapes, we select two sub-areas within the Bay area: the central region featuring a rotary interchange (Sub-area 1) and the south corridor (Sub-area 2) as illustrated in the right side of Figure 3.

For data preparation in state space reconstruction, specific preprocessing steps are executed. The z-score normalization is applied to maintain magnitude consistency across multivariate data. The embedding dimension E and positive time lag τ are calculated using false nearest

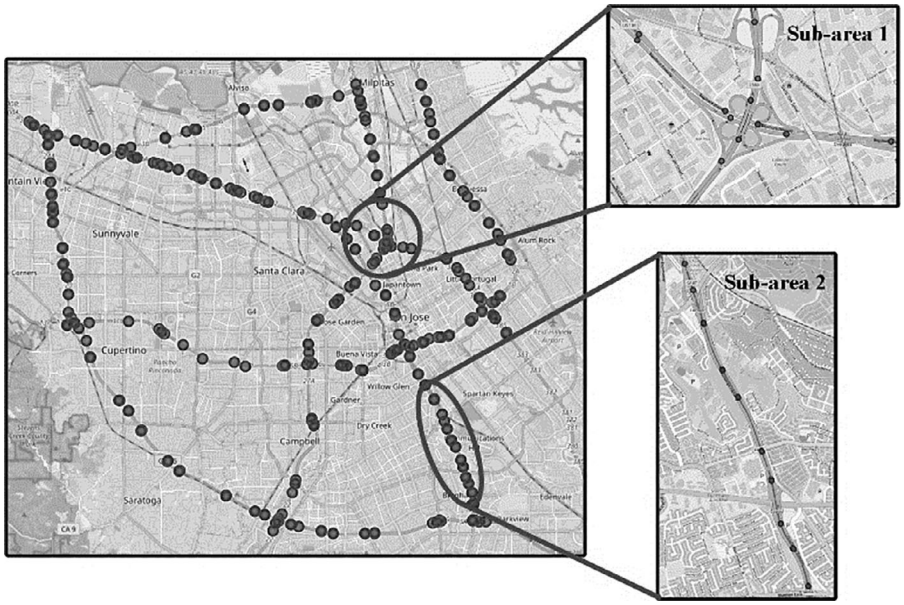

FIGURE 3 Test base and two selected areas (Sub-areas 1 and 2).

neighbors and manual information method, discussed in prior studies (Jiang & Adeli, 2003b; Vlahogianni et al., 2008). We set the embedding dimension as 5, and the positive time lag as 3, considering computational efficiency. The computational experiments were conducted on a laptop equipped with an Intel(R) Core(TM) i7-8750H CPU @ 2.20 GHz, featuring 6 cores and 16.0 GB of RAM, using Python as the programming language. The CPU execution time for the state-space reconstruction process was about 0.6 s.

3.2 | Effectiveness validation

3.2.1 | T-CCM method results on Sub-area 1

First, we focus on visualizing the results of the spatial causality coefficient in Sub-area 1 (Figure 4), to validate the effectiveness of the T-CCM method. Concretely, we designate VDS 400001 as the target sensor (marked with a yellow star in Figure 4a). For this analysis, the input time length (L) is defined as the entire duration of the time-series data, totaling 52,117, and the number of input lengths (n_t) is selected as 50. Thus , $\hat{Y}(t)|\boldsymbol{M}_S^{r_X}$ denotes the estimated shadow manifold of road r_Y with different time-length t. The causality coefficient matrix obtained with an input time length set ($\boldsymbol{t}_{L|n_t}$) is utilized for spatial causality visualization in Figure 4b, wherein the lines symbolize the causality influence scores stemming from the remaining 318 sensors to the designated target sensor.

Furthermore, the neighboring sensors of the target sensor display a color gradation ranging from yellow to deep

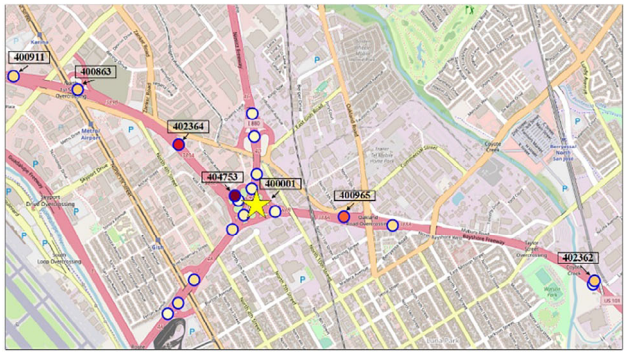

(a) Causality coefficient values visualization

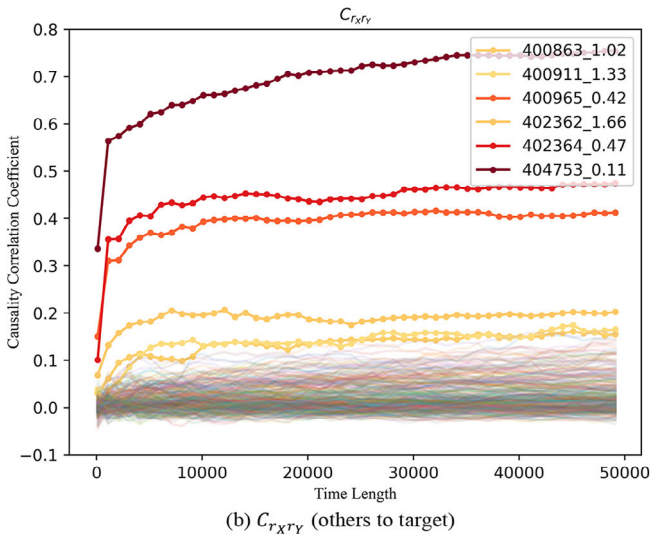

(b) $C_{r_X r_Y}$ (others to target)

FIGURE 4 Illustration of T-CCM results in Sub-area 1.

red, reflecting their corresponding convergent causality coefficient values. These labeled sensors, listed in the legends of Figure 4b and shown in Figure 4a, include each sensor's ID, which denotes the Euclidean distance in Absolute Postmiles (AbP) provided by PeMS. The figure demonstrates an approximately equal distance between upstream and downstream areas. Notably, in Figure 4b, the color of the labeled sensors gradually fades away from the target sensor, illustrating that the spatial causality diminishes with greater inter-sensor distances.

Specifically, Figure 4a clearly demonstrates the causal links between the target sensor and its upstream and downstream counterparts. In contrast, sensors in the opposite direction or along orthogonal routes of the rotary interchange exhibit no discernible causal relationships with the target sensor. This finding, which aligns with basic knowledge, suggests that, when the entire time series is employed as input, spatial causality between sensors follows a bidirectional pattern, which recedes in strength along with the expanding distance.

The illustration presented here serves as an initial glimpse into the potential of the T-CCM method for identifying spatial causality within urban traffic networks. However, there exists a compelling need for a deeper investigation into the influence of input time length and sensor positioning on spatial causality, as this exploration holds the promise of a more comprehensive understanding of the underlying dynamics inherent to the traffic network.

3.2.2 | Suitable input time length determination

Determining an appropriate input time length holds crucial significance for the efficacy of the T-CCM method, as a large input time length may create a dense shadow manifold that contains more information about the system and thus obtain more accurate spatial causality evaluation, while the longer input time length will increase the computation cost.

To this end, we select 10 distinct integer input time length values spanning evenly from 1000 to 46,000 (excluding the beginning and end of the time series) for VDS 400001 (target sensor r_X) and its immediate neighbor VDS 404753 (r_Y). Each input length value undergoes testing of T-CCM method across 100 iterations, with a number of input lengths (n_l) chosen as 20. The outcomes, $\hat{Y}(t)|\boldsymbol{M}_s^{r_X}$, depicting the causality coefficient score of r_Y on r_X, are illustrated in Figure 5. Here, the color gradient, ranging from light to dark blue, depicts varying input length values; for instance, the lightest shade of gray signifies a library length of 1000, assigned to label $\hat{Y}(t)|\boldsymbol{M}_s^{r_X} - 1$. Within this representation in Figure 5, the lines represent the median outcome derived from the iterative process, with the enveloping shadows delineating the upper and lower quartiles.

The trend underscores a robust causal relationship between VDS 400001 and 404753, manifested in rapid and convergent causality coefficient values surpassing 0.6. While the iterative results manifest slight fluctuations at around 0.06, they are nevertheless sufficient to support decisive causality inferences. Furthermore, different input lengths exhibit marginal impact on the outcomes, converging to notably high scores around the length of 2000. Remarkably, a significant revelation emerges—the input length of 2000 corresponds approximately to 1 week of traffic speed data. This realization highlights that the shadow manifold effectively encapsulates dynamic traffic insights from the road traffic system over this span.

Fortunately, the development of ITS has ushered in an era of data abundance. Leveraging this wealth of data, the T-CCM method is with heightened potential for furnishing precise causality coefficient values. As demonstrated in Figure 5, a suitable convergent input length of 7000 can be decided for the study area, ensuring a high level of causality measurement accuracy while maintaining an acceptable computation cost.

Shifting to a smaller granularity view, we present an enlarged plot in the middle of Figure 5 to gain a finer resolution within the input length range [0,800]. Notably, we identify the inflection point of the line plot for the smallest input length ($\hat{Y}(t)|\boldsymbol{M}_s^{r_X} - 1$) by a circle. These inflection points span the range of 30 to 150, leading to a rise in causality coefficient values from 0.47 to 0.55. This observation underscores the T-CCM method's aptitude in detecting spatial causality between two sensors, even with the input as few as dozens of time-series points. At the same time, this outcome verifies the method's practical utility, emphasizing its capacity to achieve convergence with a modest dataset—a concurrence in line with previous reports asserting that CCM-based methods can ascertain causality with dozens of points (Sugihara et al., 2012).

In conclusion, the present subsection illuminates crucial considerations regarding the input time length within the T-CCM framework for the detection of causality in urban traffic dynamics. Our findings underscore the method's efficacy in capturing preliminary causal relationships even with a relatively limited dataset when exploring traffic propagation dynamics. Furthermore, we identify a suitable input length of 7000 for discerning the long-term spatial causality of the whole study area, achieving a balance between the heightened precision afforded by abundant data and the necessity for computational efficiency. These insights furnish practical guidelines for the deployment of the T-CCM method in real-world scenarios, such as

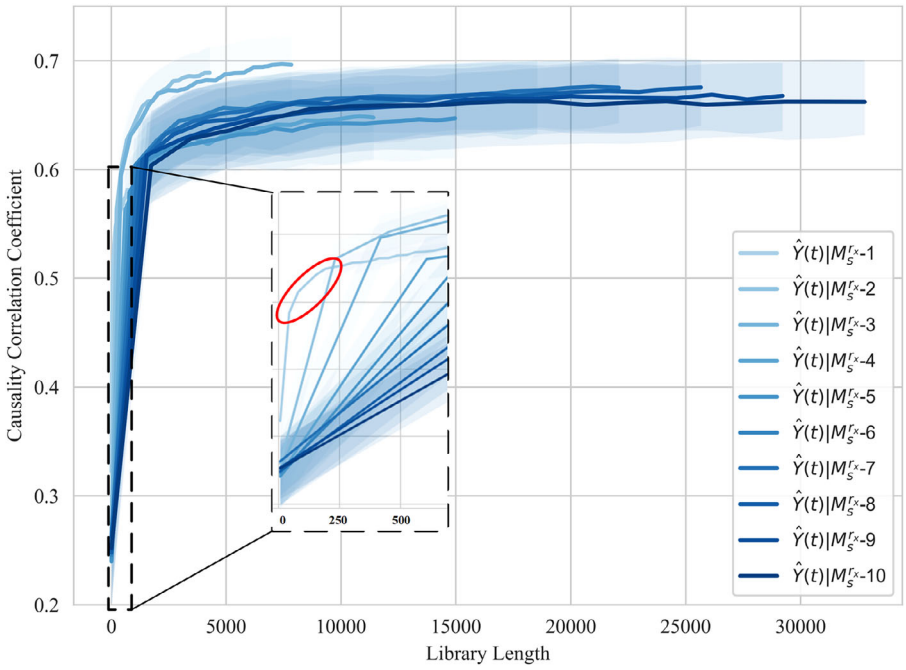

FIGURE 5 T-CCM results for different library length scenarios.

short-term traffic propagation identification and the characterization of spatial causality distribution across the network.

3.3 | Short-term causality impact: Scenarios of traffic propagation during congestion generation and dissipation in neighbor sensors

Building on the insights gained from the preceding analysis of input time length and preliminary causality identification, this section directs its attention toward detailed case studies that employ the T-CCM method to investigate dominant sensors in short-term traffic congestion propagation. Specifically, we focus on examining the causality coefficient values between upstream and downstream sensors, encompassing two distinct phases of congestion generation and dissipation during rush hours. This empirical exploration aims to provide a deeper understanding of the method's capabilities in capturing intrinsic causality patterns within the dynamic context of urban traffic.

3.3.1 | Analysis of causality effect strength in Sub-area 1

Following Section 3.2, our investigation turns to Sub-area 1, where we explore the spatial causality strength of upstream and downstream sensors in relation to the target sensor

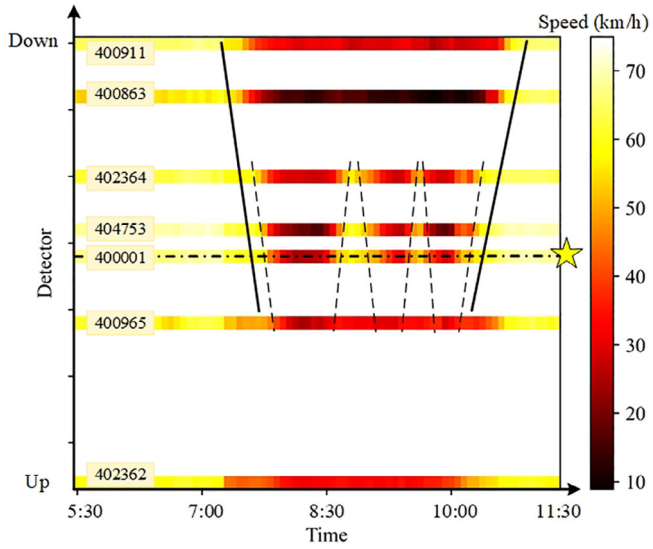

FIGURE 6 Space–time speed contour plot of Sub-area 1.

during both congestion generation and dissipation phases. This exploration centers on seven sensors aligned in one direction within Sub-area 1. Specifically, we select four downstream sensors and two upstream sensors of the target sensor, VDS 400001, to elucidate the dynamics of congestion generation and dissipation occurring between 5:30 and 11:30 a.m. on a specific day (January 25). To visualize this process, we present the time–space speed contour plot in Figure 6.

In Figure 6, the y-axis signifies the direction of traffic flow, progressing from the upstream sensor VDS402362

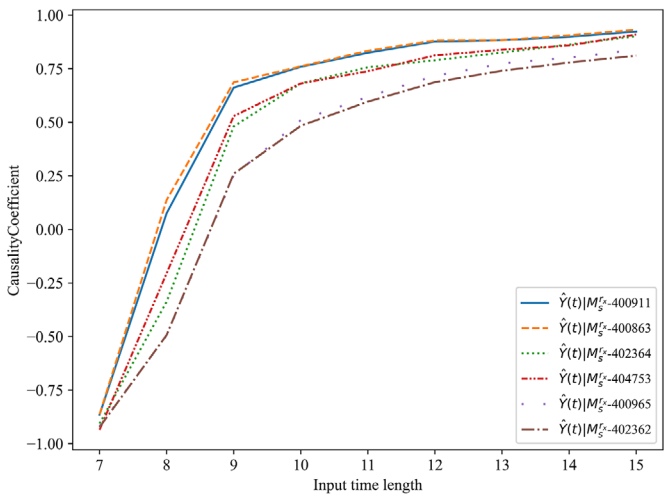

(a) T-CCM results during congestion generation (others to the target sensor in sub-area 1)

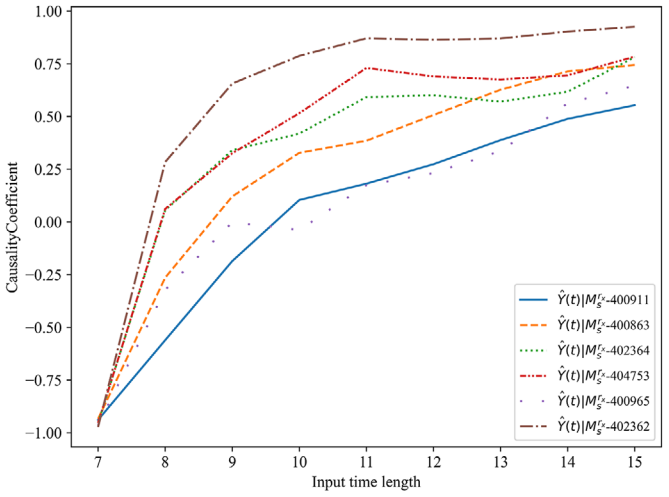

(b) T-CCM results during congestion dissipation (others to the target sensor in sub-area 1)

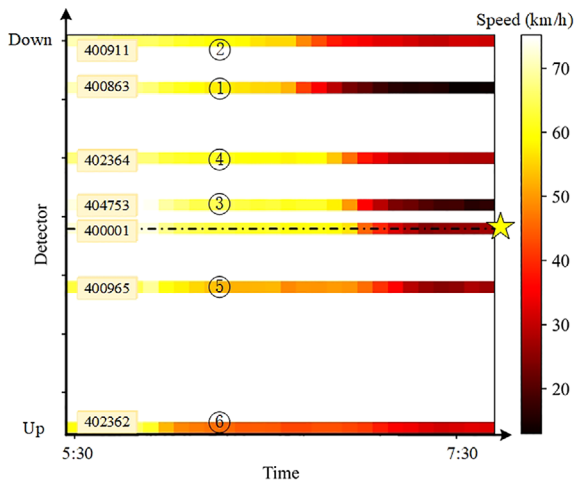

(c) Space-time speed contour plot during congestion generation (sub-area 1, 5:30 a.m. to 7:45 a.m.)

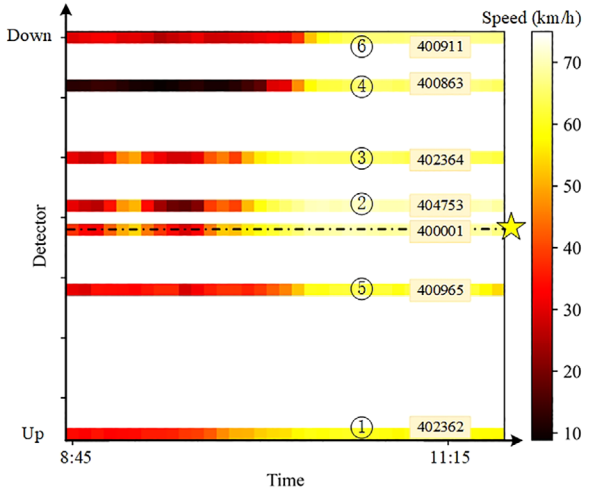

(d) Space-time speed contour plot during congestion dissipation (sub-area 1, 8:45 a.m. to 11:30 a.m.)

FIGURE 7 T-CCM results and corresponding speed contour plots regarding congestion generation and dissipation period in Sub-area 1.

to the downstream sensor VDS 400911. Notably, during the morning peak hours (7:00–10:30 a.m.), represented by solid lines, a clear pattern of speed reduction and recovery emerges. Within this interval, three minor instances of speed variation are also observed as indicated by dashed lines. It is essential to note that the location of sensors is based on relative positions derived from AbP data displayed in Figure 4. Specifically, two distinct periods are analyzed, including the congestion generation phase (5:30–7:45 a.m.) and the congestion dissipation phase (8:45–11:30 a.m.). Correspondingly, Figure 7 showcases time–space speed contour plots and the T-CCM outcomes for other sensors in relation to the target sensor during these two periods.

In the context of the congestion generation phase, Figure 7a uses different line styles to represent various sensors. It is evident that all neighbor sensors exhibit causal influences on the target sensor as reflected by convergent causality coefficient values (greater than 0.75) with increasing input time length from 7 to 15. Noteworthy is the observation that the downstream sensor VDS 400863, depicted by the dashed line, holds the most pronounced causal influence on the target sensor. Conversely, the head upstream sensor VDS 402362, indicated by the dash-dot line, exerts the weakest influence. To offer a clear representation of causal impact, Figure 7c arranges sensors' causality coefficient values in descending order, underscored by labels within the time–space speed counter plot. This sorting confirms that, during the congestion generation phase, downstream sensors exert a stronger influence, compared to upstream counterparts. In this context, congestion originating from downstream sensors induces a backward congestion wave, affecting upstream sensors. Intriguingly, VDS 400863 holds the highest causal

influence on the target sensor, slightly surpassing the head downstream sensor VDS 400911. This discrepancy can be attributed to VDS 400863's speed valley at around 20 km/h, resulting in a bottleneck phenomenon that triggers this congestion episode.

Transitioning to the congestion dissipation phase, Figure 7b,d displays a different circumstance. The primary causal impacts on the target sensor now stem from the leading upstream sensor VDS 402362, with the trailing downstream sensor VDS 400911 occupying the lowest rank. This discrepancy suggests that downstream causal effects dominate during congestion generation, while upstream effects gain prominence during congestion dissipation. However, during the congestion dissipation period in Sub-area 1, there are three instances of self-organized generation-dissipation behavior as highlighted in Figure 6. The speed contour plot reveals recurring congestion waves over time, marked by dashed lines, and variations in traffic states that are especially pronounced around the middle three sensors (VDS 404753, 400001, and 400965), which are situated at the rotary interchange or at connections between the highway and urban roads. While short-term fluctuations at these critical points do impact traffic patterns, they do not undermine the overall reliability of our causality analysis over extended congestion periods. Addressing this complexity, we turn our focus to Sub-area 2, a more straightforward and intuitive research area concentrating on a section of a highway corridor.

Mover, a comparative analysis was conducted between our method and established approaches, namely, spatial dependency correlation measurement and the Granger causality method. For spatial dependency correlation, the identical calculation process was utilized, and results were normalized to the range [0,1]. Regarding the Granger causality method, lag order selection was based on the Akaike Information Criterion, with the *F*-test applied to determine causal strength. For both methods, a 5% significance level ($p < .05$) was established as the benchmark for determining significance, while correlation values and *F*-statistics were used to quantify the strength of the relationships. The results of these two methods for Sub-area 1 are listed in Table 2.

Quantification results from both comparison methods are presented in Table 2, with the strongest relationships to the target sensor 400001 highlighted in bold. Spatial correlation measurement tends to identify the nearest sensors as having strong correlations (strong similarity), whereas the Granger causality method is even less effective. During the congestion generation period, Granger causality test results indicate that 402364 (not the actual speed valley 400863 shown in Figure 7) exhibits the strongest causal connection to the target sensor, with the head upstream sensor 402362 ranking second. In the congestion dissipation period, the Granger causality test finds no causal links between the target sensor and its upstream/downstream sensors. Clearly, system uncertainty and sensor interdependency cause these methods to misidentify causality.

TABLE 2 Comparison results in Sub-area 1.

Sensor ID	Congestion generation		Congestion dissipation	
	Spatial correlation	Granger causality	Spatial correlation	Granger causality
400911	–	–	–	–
400863	–	–	–	–
402364	0.459	**12.768**	0.834	–
404753	**0.863**	5.323	**0.902**	–
400965	0.726	–	–	–
402362	–	7.880	–	–

3.3.2 | Analysis of causality effect strength in Sub-area 2

The focus of this part shifts to Sub-area 2, situated in the southern region of the PeMS-Bay area. Sub-area 2 is a corridor channel that directs traffic flow from south to north as illustrated in Figure 8. Sub-area 2 comprises eight sensors, including the target sensor VDS 400178, along with three upstream and four downstream sensors. The chosen analysis period, encompassing both congestion generation and dissipation, spans from 5:00 to 11:00 a.m. on April 3. The speed contour plot depicted on the right side of Figure 8 presents a consistent pattern of speed drop and subsequent increase from the head downstream sensor VDS 400654 to the head upstream sensor VDS 401129.

Analogous to Section 3.3.1, we analyze the causal impacts of upstream and downstream sensors on the target sensor during both congestion generation and dissipation phases. For the congestion generation period, Figure 9a,c depicts T-CCM results and corresponding speed contour plots, complemented by causal strength rankings within Sub-area 2. Figure 9a highlights the most influential sensor, VDS 400418 (dashed line), which emerges as the dominant influencer with a causality coefficient value of around 0.8. Conversely, the upstream sensor VDS 404451 (loosely dotted line) exerts a least pronounced influence as indicated by its causality coefficient value below 0. Moreover, Figure 9c underscores that all four downstream sensors wield a more substantial impact on the target sensor, boasting causality coefficient values exceeding 0.75. As for the congestion dissipation phase, Figure 9b,d presents a shift in the spatial causality impact. In this scenario, the three upstream sensors (VDS 401129, 401957, and 404451) now lead to exerting causal effects on the target sensor, each possessing a causality coefficient value around or

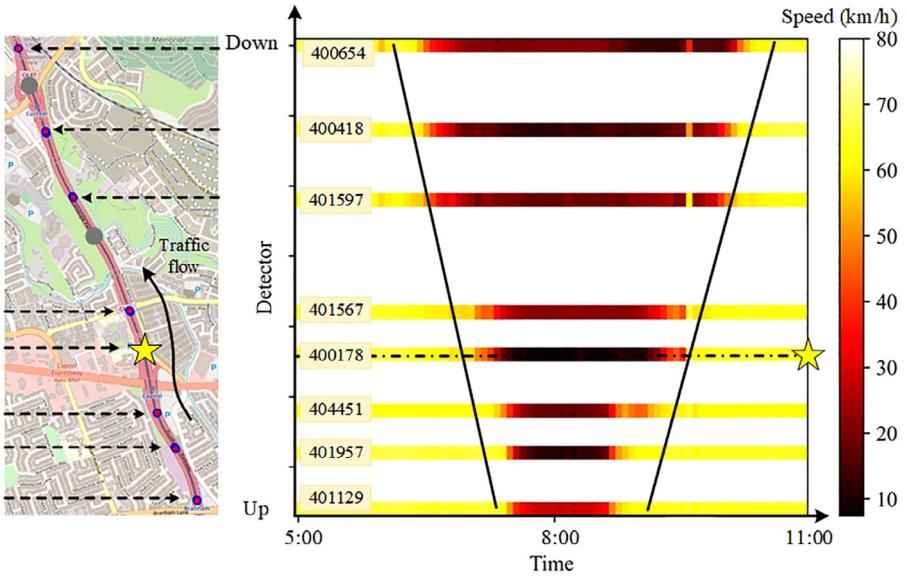

FIGURE 8 Sensor location information and space-time speed contour plot of Sub-area 2.

exceeding 0.6. This outcome aligns with the inference drawn in Section 3.3.1.

To distill our findings, we discern that, from a causality perspective derived from traffic speed data, congestion generation predominantly entails a downstream change in velocity, culminating in a more substantial causal linkage with the target sensor. Conversely, congestion dissipation initiates with an upstream speed raise, thereby accentuating the causal impact of upstream sensors on the target. This alignment with established traffic flow theory, particularly kinematic wave theory, underscores the interaction between nearby sensors through kinematic waves (Coclite et al., 2005; Jin, 2012; Jin et al., 2015; Kim & Cassidy, 2012).

Delving deeper, an examination of sensors with the most robust causal effect strength on the target sensor in each period discloses notable insights. During the congestion generation period, VDS 400418 commands the highest causal effect strength, marginally surpassing its downstream sensor VDS 400654. This discrepancy arises due to the presence of an off-ramp near VDS 400418 as can be seen in the road illustration of Figure 9c. This off-ramp may cause lane changes and ramp queues, contributing to VDS 400418's heightened and more direct influence on the target sensor, although the congestion originates from VDS 400654.

Transitioning to the congestion dissipation phase, compared with the other two upstream sensors of the target sensor, the most influential sensor, VDS 404451, exhibits a higher causality coefficient value of approximately 0.75 (loosely dotted line in Figure 9b). This variation can be attributed to the off-ramp positioned near VDS 404451. The smoother and more consistent traffic flow between the two upstream sensors (VDS 401129, 401957) is perturbed by the off-ramp near VDS 404451, inducing a distinctive flow configuration. Thus, during the congestion dissipation period, VDS 404451 assumes the mantle of spatial causality impact on the target sensor.

TABLE 3 Comparison results in Sub-area 2.

Sensor ID	Congestion generation		Congestion dissipation	
	Spatial correlation	Granger causality	Spatial correlation	Granger causality
400654	–	–	0.524	3.802
400418	–	–	0.657	–
401597	–	–	0.669	**4.526**
401567	**0.851**	–	**0.98**	–
404451	0.348	–	0.362	–
401957	–	–	–	–
401129	–	–	–	–

The spatial correlation and Granger causality test are also tested in Sub-area 2, shown in Table 3. In the less complex scenario of Sub-area 2, spatial correlation continues to identify only the nearest sensor linkages and further selects downstream sensors with patterns similar to the target sensor 400178 during congestion dissipation. Granger causality still shows its weakness in non-independent systems, failing to identify any sensor with a causal relationship to the target during the congestion generation period. Additionally, we evaluate these methods in a more deterministic network scenario detailed in Appendix A, featuring a network system with well-defined traffic inputs and vehicle routes.

Moreover, a comprehensive understanding of sensor interactions along the corridor in Sub-area 2 prompts further analysis of inter-causal effects between every sensor

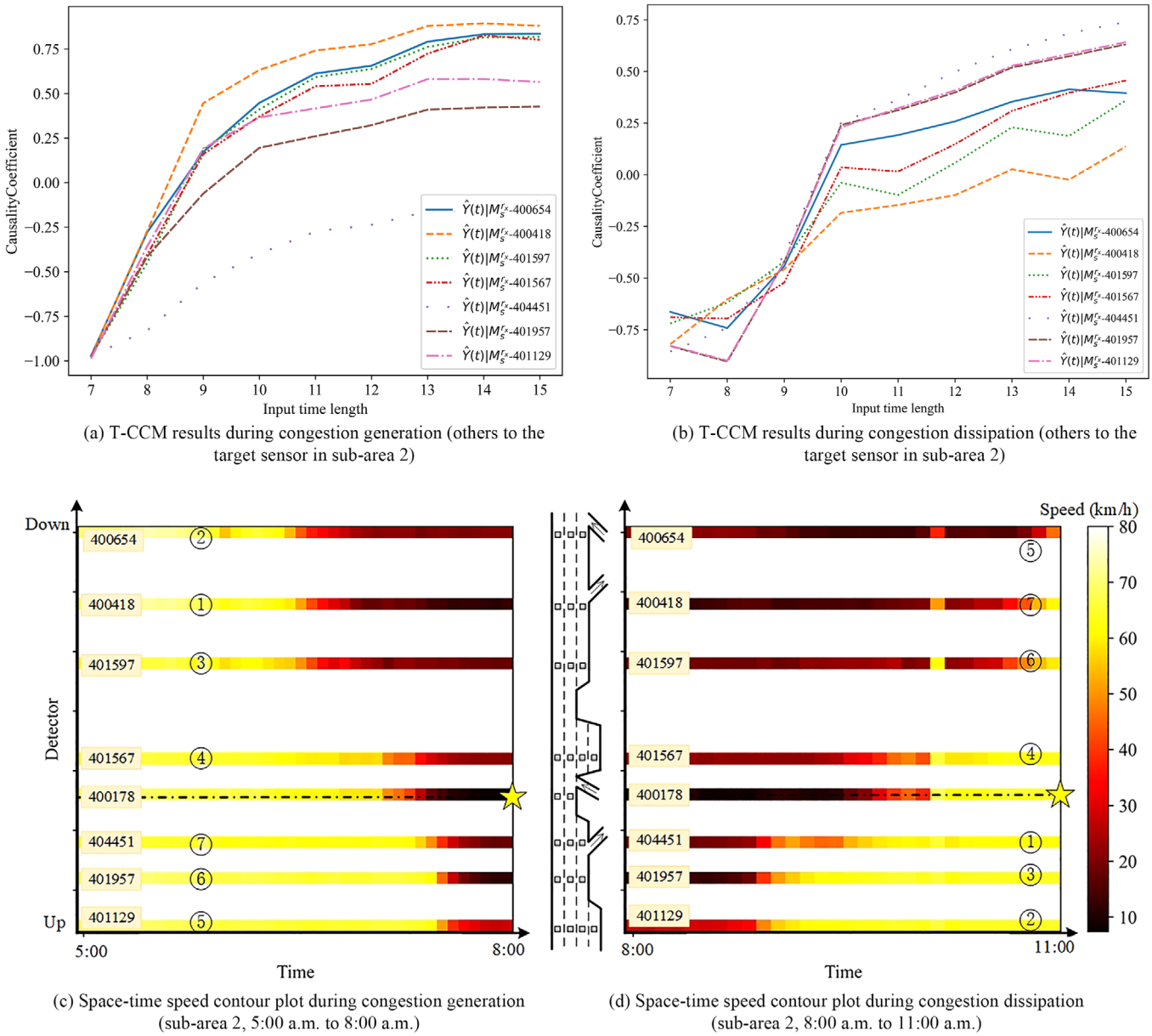

(a) T-CCM results during congestion generation (others to the target sensor in sub-area 2)

(b) T-CCM results during congestion dissipation (others to the target sensor in sub-area 2)

(c) Space-time speed contour plot during congestion generation (sub-area 2, 5:00 a.m. to 8:00 a.m.)

(d) Space-time speed contour plot during congestion dissipation (sub-area 2, 8:00 a.m. to 11:00 a.m.)

FIGURE 9 T-CCM results and corresponding speed contour plots regarding congestion generation and dissipation period in Sub-area 2.

pair during both congestion generation and dissipation periods as depicted in the heatmap of Figure 10. In this heatmap, each row signifies the influencer, each column represents the affected sensor, and the shade of each square denotes the strength of causality influence. For instance, Row 3 and Column 5 correspond to the causality effects from VDS 401597 to VDS 400178, ranking fourth in the influence values from VDS 401597 to others.

In Figure 10a,b, the solid ellipse and line boxes delineate the dominant sensor and sensor clusters during congestion generation and dissipation periods, respectively. It is noteworthy that VDS 400418 and 404451 continue to hold sway over causality impacts on other sensors during congestion generation and dissipation phases. In this case, these two sensors, located near off-ramps, assume the role of diverge bottlenecks (D. Chen & Ahn, 2018) that frequently emerge in recurrent congestion scenarios (Spiliopoulou et al., 2014) and may even deteriorate traffic flow more than on-ramp bottleneck (Munoz & Daganzo, 2002). Furthermore, a clustering phenomenon surfaces among inter-causal effects. Notably, during the congestion generation period (Figure 10a), the group of sensors, marked in the solid box, has stronger causality impacts within each other than the other group that is marked in the dashed box. This pattern reverses during the congestion dissipation period as illustrated in Figure 10b.

In light of the aforementioned analysis, it becomes evident that traffic flow merging and diverging, along with

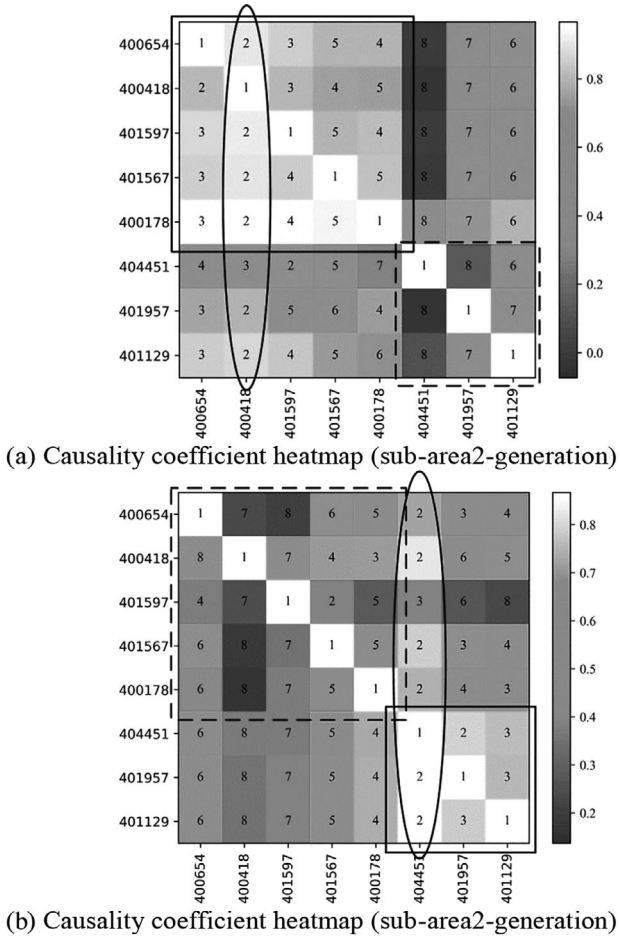

(a) Causality coefficient heatmap (sub-area2-generation)

(b) Causality coefficient heatmap (sub-area2-generation)

FIGURE 10 Inter-causal effects between every two sensors.

their spatial distribution, give rise to intricate scenarios in traffic flow analysis. This underscores the limitations of conventional traffic flow analysis in handling complex real-world traffic conditions. Nevertheless, drawing from the analyses of Sub-areas 1 and 2, spatial causality analysis effectively captures the influence of traffic merging and diverging on upstream and downstream sensors.

3.4 | Long-term causality impact: T-CCM results across the entire network

This section will discuss the long-term spatial causality impact by applying the T-CCM method to the entirety of the PeMS-Bay dataset, encompassing 318 sensors. While earlier sections concentrated on the short-term causal impact among nearby sensors, this section necessitates a discussion of the extensive causal influence throughout the network. Specifically, as the fundamental causal connections between nearby sensors were expounded upon in Section 3.3, a secondary layer of causality, generated by long-term traffic propagation and intertwined with factors such as vehicle travel preferences, land usage, and POIs, may also come into play. This intricate scenario will be elucidated in the following.

3.4.1 | Parameter configurations

For the whole network spatial causality analysis, we establish the input time length L at 7000 (approximately a month), based on prior analyses and given the focus on investigating long-term causal impacts between sensors. The step size n_t is set to 1, as a high causality coefficient value with an input time length of 7000 can ensure the existence of causal effects between pairs of sensors to some degree. Consequently, the causality coefficient calculation will be computed once for each sensor pair, resulting in a causality matrix $\mathbf{C}_{nn}^{\mathbf{t}_L}$ derived from an input time length of 7000.

Furthermore, we incorporate a threshold of 0.2 for causality values to filter out inconsequential disturbances in $\mathbf{C}_{nn}^{\mathbf{t}_L}$. The refined causality matrix $\mathbf{C}_{nn}^{\mathbf{t}_L}|_{0.2}$ is then employed to construct a weighted directed graph denoted as $G = (\mathbf{V}, \mathbf{E}, \mathbf{W})$, where $\mathbf{V}, \mathbf{E}, \mathbf{W}$ are the sensor set, causality interaction link set, and the link strength (causality coefficient value) set, respectively. Assuming two sensors, r_x and r_y, exhibit a causal relationship from r_x to r_y. The causality coefficient value can be interpreted as the link strength from r_x to r_y. Moreover, the weighted direct graph derived from the refined causality matrix $\mathbf{C}_{nn}^{\mathbf{t}_L}|_{0.2}$ empowers us to gauge the influence of each sensor through its out-degree, reflecting its capability to influence others, and its in-degree, illuminating its susceptibility to causal impact from other sensors. This weighted direct graph offers an intuitive visualization of the intricate interplay among network sensors in terms of spatial causality relationships.

3.4.2 | Spatial distribution of causality coefficient values in the network

Illustrated in Figure 11, the spatial distribution outcomes unveil a comprehensive view of the network causal interconnections. Each node within the graph corresponds to a sensor, and the color spectrum, transitioning from blue to red, signifies the ascending node degree, with larger nodes indicating higher degrees. The links between nodes are equally elucidated: Stronger causality interactions are depicted by broader and deeper blue lines.

Specifically, Figure 11a,b displays the spatial distribution of in-degree and out-degree, respectively. Noteworthy sensors with substantial in-degree or out-degree are delineated by boxes, and a discernible divergence in the spatial distribution patterns of in-degree and out-degree is evident. For the two black boxes, black box 1, with high

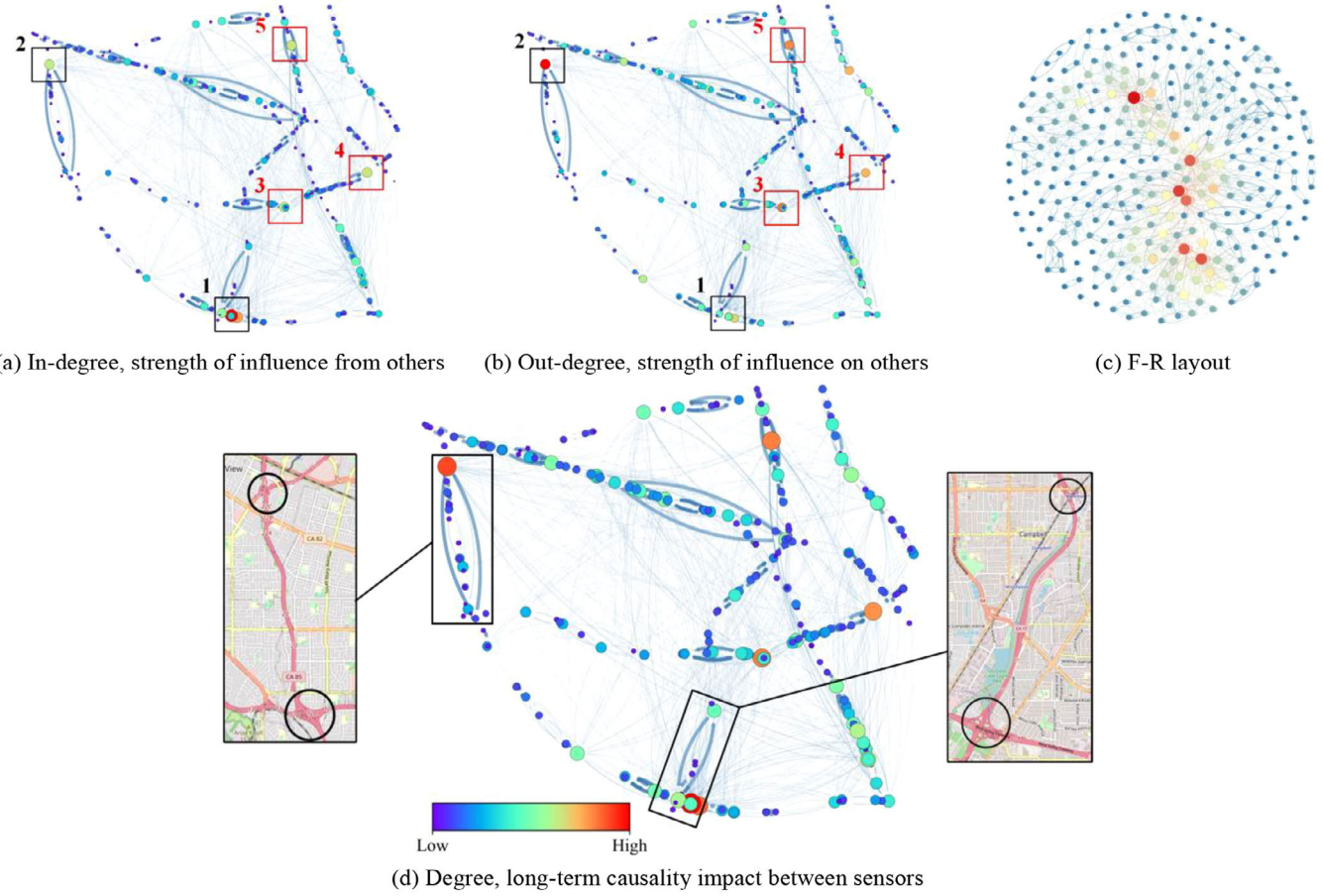

(a) In-degree, strength of influence from others (b) Out-degree, strength of influence on others (c) F-R layout

(d) Degree, long-term causality impact between sensors

FIGURE 11 Spatial distribution of causality values.

in-degree and relatively lower out-degree, contrasts with the scenario in black box 2. Given the multitude of sensors exercising causality effects from other sensors (Figure 11a), it is reasonable to infer it as the principal egress of the PeMS-Bay network—pointing to it as the key outlet for departing vehicles. Similarly, black box 2, distinguished by the highest out-degree in Figure 11b, serves as the prominent entry point into the PeMS-Bay network.

Regarding red box areas, they also exhibit notable in-degree and out-degree values. For instance, the vicinity of red box 3, located at the junction of three major arterials, yields high in-degree and out-degree values. Red box 4 contains a composite site comprising a park, zoo, and commercial center. As for the red box 5 area, there are some residential places and a big mobile home park. The POIs and land use of these three areas permit traffic to converge and diverge, consequently leading to high in-degree and out-degree values.

Furthermore, Figure 11c,d depicts the Fruterman–Reingold (F-R) layout (Fruchterman & Reingold, 1991) and the cumulative degree values (in-degree plus out-degree), respectively. The F-R layout can minimize the energy of the graph system and illustrate a compact spatial layout without changing the topology structure (Yang et al., 2019). Figure 11c clearly outlines that most sensors have low degree values, while high-degree sensors cluster and form distinct groupings. It is not surprising that aggregation and clustering occur, as spatial causation stemming from traffic speed is a kind of reflection of urban traffic propagation. Urban road traffic fundamentally entails the propagation of traffic along roadways, and the inherent interdependency of roads is clearly reflected through the F-R layout's preservation of the topology structure. These road clusters can be regarded as the principal contributing roads that approximately characterize the dynamic system of the PeMS-Bay area.

In Figure 11d, the degree plot is consistent with in-degree and out-degree plots. Concerning links in the graph, wide-width and deep-color links manifest between adjacent sensors, with the exception of a limited number of distinctive cases from distant sensors. These specific cases are exemplified in two magnified sample regions of Figure 11d, where each pair of sensors with strong causality interactions is marked by a black circle. These sensor pairs correspond to two important adjacent junctions along the main highway. Therefore, strong causality interactions can

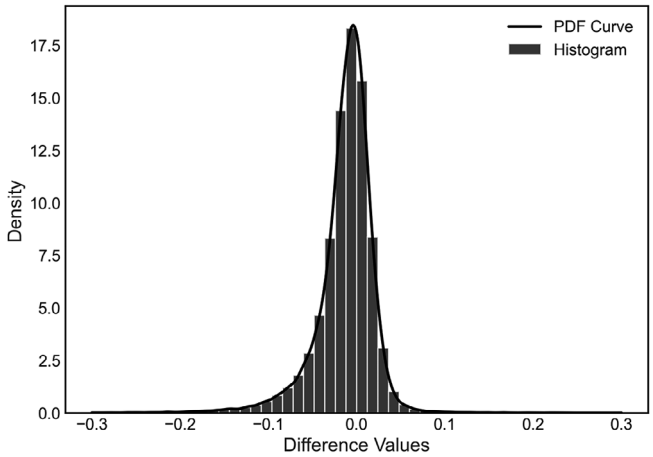

FIGURE 12 Histogram of matrix differences with Probability Density Function (PDF) curve.

be observed, which can be attributed to consistent route preferences of the drivers.

In addition to the initial 1-month analysis, an extended study is conducted over a 3-month period to further validate the robustness of our causality assessment across longer time frames. This comprehensive analysis involved recalculating the causality matrix using the extended PeMS dataset. The histogram distribution of matrix differences, depicted in Figure 12, demonstrates that the majority of differences are narrowly centered around zero, indicating minimal variation and confirming the robustness of our method over varying time frames. This finding substantiates the stability of our causality assessments, reinforcing that a 1-month horizon is sufficiently representative for analyzing urban traffic dynamics in the chosen study area, as discussed in Section 3.2.2.

Beyond short-term causal relationships evident in shorter timeframes, this analysis uncovers a deeper layer of spatial causality with longer time periods and influenced by travelers (travel behavior), the spatial distribution of urban functions (land use), and the attractiveness of specific locations (POIs). Long-term causality relationships established across extended temporal horizons encapsulate the enduring effects of these factors on urban traffic dynamics. Understanding these long-term influences enhances the comprehension of the underlying dynamics in urban traffic networks, enabling urban planners and policymakers to make well-informed decisions for the optimization of transportation systems and the enhancement of overall urban mobility.

3.5 | Discussions and limitations

The uncertainty and interdependency intrinsic to dynamic urban traffic systems pose challenges to the comprehensive analysis of traffic flow dynamics. In traffic systems, uncertainty emerges as a foundational characteristic due to the inherently complex and dynamic nature of urban traffic. The interdependency of roads intensifies the complexities, making the information from influential sensors inseparable from the target sensor during traffic propagation. This underscores the limitations inherent in conventional analytical approaches and Granger causality frameworks, which may struggle in measuring uncertainty and may neglect interdependencies among sensors.

In this context, simulations, while valuable for theoretical analysis and controlled environment testing, may fail to capture the multi-dimensional interactions of actual, real-sized urban networks and may oversimplify or constrain inherent complexities. Our method leverages limited time-series data from these complex systems to reconstruct large-scale traffic dynamics effectively. This approach ensures that our methodology is immediately applicable and validated for practical use in existing urban infrastructures, offering a direct application advantage without the need for constructing simulation environments or making extensive adjustments.

Furthermore, this uncertainty and interdependency often result in information propagating bidirectionally through time (Ye, Deyle, et al., 2015), analogous to the dynamical interaction between upstream and downstream sensors in traffic systems. This complexity is further compounded in congestion scenarios, where a traffic bottleneck can trigger various effects, as detailed in previous work (Kim & Cassidy, 2012). The proposed T-CCM method offers a promising solution to tackle these challenges. With the help of state-space reconstruction, T-CCM approaches the mining of interaction strengths between sensors, particularly causality influence, from a distinct perspective. The analyses of short-term and long-term causality impacts clearly demonstrate the method's efficacy in solving the intricacies caused by uncertainty and interdependency, thereby advancing the capacity to comprehend and navigate the complexities inherent in dynamic urban traffic systems.

However, as the T-CCM method relies exclusively on time-series data, the length and nature of the input time series significantly influence its outcomes. Analyzing different time lengths reveals varied scenarios: micro situations involve congestion propagation through nearby sensors and are represented by short-term causality impacts, whereas macro situations reflect long-term causality impacts and relate to travel choices over extended periods. Additionally, the potential for spurious dependencies due to coincidental similarities in time-series data poses a challenge. To address these, the T-CCM method can be enhanced by incorporating additional system properties such as network topology and the frequency of

time-series data. Integrating these properties aims to refine the exploration of spatial causality and better align the detection of causal relationships with the physical and operational realities of urban traffic networks.

4 | CONCLUSION

This paper designs a spatial causality detection framework, termed T-CCM, tailored to reveal the spatial causal relationships among road segments within a given road network, while considering the dynamic propagation of traffic. Leveraging the principles of state-space reconstruction, T-CCM employs network traffic time-series data as input to quantify the degree to which the state space of a target road, as formed by its time-series data, can be effectively used to reconstruct those of other roads. This quantification can measure the causality impacts originating from these other roads and directed toward the target road. Notably, T-CCM operates exclusively with traffic time-series data as input and is capable of identifying spatial causal relationships under the constraints of uncertainty and interdependency inherent to dynamic traffic systems.

The application of our method empowers transportation policymakers and management staff with a tool to develop advanced congestion mitigation strategies, even with access to only basic traffic time-series data. This is particularly valuable for roads exhibiting high causality coefficient values, which indicate intense and frequent interactions with other segments. Through experiments conducted on real-world PeMS data, we have demonstrated the method's ability to identify bidirectional causal effects during congestion generation and dissipation within short-term periods. Moreover, our method can reproduce the dominant causal impacts of off-ramps in the diverging traffic. Importantly, when considering long-term time periods, T-CCM uncovers a deeper layer of spatial causality relating to travel behavior and road land use attributes by accounting for a broader impact range.

In short-term applications, this method is useful in real-time traffic management by enabling quick responses to accidents or congestion by identifying origins, impacted areas, and bottlenecks (C. Li et al., 2020). Important roads or bottlenecks can be identified according to sensors/roads exhibiting high causality coefficient values, which indicates their significant impact on congestion. See Appendix B for further discussions.

In general, understanding the relationship between roads has significant implications for short-term traffic management, particularly in short-term traffic prediction, which has been a focal point of research in recent years. Studies by L. Li et al. (2015) and Mao et al. (2022) demonstrate that analyzing inter-road relationships enhances prediction models by selecting appropriate inputs and excluding irrelevant data, thereby reducing system complexity and improving accuracy. This approach supports real-time traffic management by enabling swift responses to accidents or congestion. Additionally, within the connected automated vehicles framework, this method can identify key vehicles for information exchange, ensuring robust and effective decision-making processes (Shi et al., 2022).

Long-term applications benefit from quantifying the long-term causal relationships, offering valuable insights into the current urban land-use distribution and regional traveler behaviors. The planning community can identify potential congestion areas (Wu et al., 2020) and important roads in terms of network vulnerability (Gu et al., 2023). Furthermore, this information can inform transportation infrastructure investments, prioritizing areas for network modification and public transit improvements.

Future research will focus on applying the T-CCM algorithm to image and video traffic data, leveraging convolutional neural networks to convert visual data from each timestamp into a time-series format. Additionally, extending the current framework to include anomaly detection (Adeli & Karim, 2005; Karim & Adeli, 2003) is a considered application. Developing an efficient method for parameter calibration in state-space reconstruction is essential, particularly for diverse operational conditions like work zones (Adeli & Ghosh-Dastidar, 2004; Y. Chen, Yang, et al., 2022; Hooshdar & Adeli, 2004; Jiang & Adeli, 2003a). Further, given the appropriate time-series data, T-CCM can be adapted to analyze queue dynamics, offering insights into the evolution of system delays and queue length fluctuations over time.

ACKNOWLEDGMENTS

This work was supported by the National Natural Science Foundation of China (Grant Number 52102376; Grant number 62103292), Fundamental Research Funds for the Central Universities (Grant number 2242022R40055).

REFERENCES

Adeli, H., & Ghosh-Dastidar, S. (2004). Mesoscopic-wavelet freeway work zone flow and congestion feature extraction model. *Journal of Transportation Engineering*, *130*(1), 94–103.

Adeli, H., & Karim, A. (2005). *Wavelets in intelligent transportation systems*. John Wiley & Sons, Inc.

Boquet, G., Morell, A., Serrano, J., & Vicario, J. L. (2020). A variational autoencoder solution for road traffic forecasting systems: Missing data imputation, dimension reduction, model selection and anomaly detection. *Transportation Research Part C: Emerging Technologies*, *115*, 102622.

Celikoglu, H. B., & Silgu, M. A. (2016). Extension of traffic flow pattern dynamic classification by a macroscopic model using multivariate clustering. *Transportation Science*, *50*(3), 966–981.

Chen, D., & Ahn, S. (2018). Capacity-drop at extended bottlenecks: Merge, diverge, and weave. *Transportation Research Part B: Methodological*, *108*, 1–20.

Chen, W., Chen, L., Xie, Y., Cao, W., Gao, Y., & Feng, X. (2020). Multi-range attentive bicomponent graph convolutional network for traffic forecasting. *Proceedings of the AAAI Conference on Artificial Intelligence*, *34*(4), 3529–3536.

Chen, Y., Mao, J., Zhang, Z., Huang, H., Lu, W., Yan, Q., & Liu, L. (2022). A quasi-contagion process modeling and characteristic analysis for real-world urban traffic network congestion patterns. *Physica A: Statistical Mechanics and its Applications*, *603*, 127729.

Chen, Y., Yang, D., Jia, B., Zhou, C., Ma, D., Liu, W., & Gu, J. (2022). Traffic wave models for the urban road with a work zone. *Transportation Letters*, *14*(6), 675–684.

Cheng, Q., Liu, Z., Guo, J., Wu, X., Pendyala, R., Belezamo, B., & Zhou, X. S. (2022). Estimating key traffic state parameters through parsimonious spatial queue models. *Transportation Research Part C: Emerging Technologies*, *137*, 103596.

Coclite, G. M., Garavello, M., & Piccoli, B. (2005). Traffic flow on a road network. *SIAM Journal on Mathematical Analysis*, *36*(6), 1862–1886.

Daganzo, C. F. (1995). Requiem for second-order fluid approximations of traffic flow. *Transportation Research Part B: Methodological*, *29*(4), 277–286.

Dai, X., Fu, R., Zhao, E., Zhang, Z., Lin, Y., Wang, F.-Y., & Li, L. (2019). DeepTrend 2.0: A light-weighted multi-scale traffic prediction model using detrending. *Transportation Research Part C: Emerging Technologies*, *103*, 142–157.

Deyle, E. R., May, R. M., Munch, S. B., & Sugihara, G. (2016). Tracking and forecasting ecosystem interactions in real time. *Proceedings of the Royal Society B: Biological Sciences*, *283*(1822), 20152258.

Fruchterman, T. M., & Reingold, E. M. (1991). Graph drawing by force-directed placement. *Software: Practice and Experience*, *21*(11), 1129–1164.

Ge, X., & Lin, A. (2022). Kernel change point detection based on convergent cross mapping. *Communications in Nonlinear Science and Numerical Simulation*, *109*, 106318.

Ghosh-Dastidar, S., & Adeli, H. (2006). Neural network-wavelet microsimulation model for delay and queue length estimation at freeway work zones. *Journal of Transportation Engineering*, *132*(4), 331–341.

Granger, C. W. (1969). Investigating causal relations by econometric models and cross-spectral methods. *Econometrica: Journal of the Econometric Society*, *37*, 424–438.

Gu, Y., Chen, A., & Xu, X. (2023). Measurement and ranking of important link combinations in the analysis of transportation network vulnerability envelope buffers under multiple-link disruptions. *Transportation Research Part B: Methodological*, *167*, 118–144.

Habtemichael, F. G., & Cetin, M. (2016). Short-term traffic flow rate forecasting based on identifying similar traffic patterns. *Transportation Research Part C: Emerging Technologies*, *66*, 61–78.

Hooshdar, S., & Adeli, H. (2004). Toward intelligent variable message signs in freeway work zones: Neural network model. *Journal of Transportation Engineering*, *130*(1), 83–93.

Huang, G., Qiao, S., & Yeh, A. G.-O. (2021). Spatiotemporally heterogeneous willingness to ridesplitting and its relationship with the built environment: A case study in Chengdu, China. *Transportation Research Part C: Emerging Technologies*, *133*, 103425.

Huang, H., Mao, J., Lu, W., Hu, G., & Liu, L. (2023). DEASeq2Seq: An attention based sequence to sequence model for short-term metro passenger flow prediction within decomposition-ensemble strategy. *Transportation Research Part C: Emerging Technologies*, *146*, 103965.

Jiang, X., & Adeli, H. (2003a). Freeway work zone traffic delay and cost optimization model. *Journal of Transportation Engineering*, *129*(3), 230–241.

Jiang, X., & Adeli, H. (2003b). Fuzzy clustering approach for accurate embedding dimension identification in chaotic time series. *Integrated Computer-Aided Engineering*, *10*(3), 287–302.

Jiang, X., & Adeli, H. (2004). Object-oriented model for freeway work zone capacity and queue delay estimation. *Computer-Aided Civil and Infrastructure Engineering*, *19*(2), 144–156.

Jin, W.-L. (2012). A kinematic wave theory of multi-commodity network traffic flow. *Transportation Research Part B: Methodological*, *46*(8), 1000–1022.

Jin, W.-L. (2021). A link queue model of network traffic flow. *Transportation Science*, *55*(2), 436–455.

Jin, W.-L., Gan, Q.-J., & Lebacque, J.-P. (2015). A kinematic wave theory of capacity drop. *Transportation Research Part B: Methodological*, *81*, 316–329.

Karim, A., & Adeli, H. (2003). Fast automatic incident detection on urban and rural freeways using wavelet energy algorithm. *Journal of Transportation Engineering*, *129*(1), 57–68.

Ke, J., Qin, X., Yang, H., Zheng, Z., Zhu, Z., & Ye, J. (2021). Predicting origin-destination ride-sourcing demand with a spatio-temporal encoder-decoder residual multi-graph convolutional network. *Transportation Research Part C: Emerging Technologies*, *122*, 102858.

Kim, K., & Cassidy, M. J. (2012). A capacity-increasing mechanism in freeway traffic. *Transportation Research Part B: Methodological*, *46*(9), 1260–1272.

Kuznetsov, N. V., Mokaev, T. N., Kuznetsova, O. A., & Kudryashova, E. V. (2020). The Lorenz system: Hidden boundary of practical stability and the Lyapunov dimension. *Nonlinear Dynamics*, *102*, 713–732.

Leng, S., Ma, H., Kurths, J., Lai, Y.-C., Lin, W., Aihara, K., & Chen, L. (2020). Partial cross mapping eliminates indirect causal influences. *Nature Communications*, *11*(1), 1–9.

Li, C., Yue, W., Mao, G., & Xu, Z. (2020). Congestion propagation based bottleneck identification in urban road networks. *IEEE Transactions on Vehicular Technology*, *69*(5), 4827–4841.

Li, L., Su, X., Wang, Y., Lin, Y., Li, Z., & Li, Y. (2015). Robust causal dependence mining in big data network and its application to traffic flow predictions. *Transportation Research Part C: Emerging Technologies*, *58*, 292–307.

Li, Y., Yu, R., Shahabi, C., & Liu, Y. (2017). *Diffusion convolutional recurrent neural network: Data-driven traffic forecasting*. ArXiv. https://arxiv.org/abs/1707.01926

Lighthill, M. J., & Whitham, G. B. (1955). On kinematic waves II. A theory of traffic flow on long crowded roads. *Proceedings of the Royal Society of London. Series A. Mathematical and Physical Sciences*, *229*(1178), 317–345.

Mao, J., Huang, H., Lu, W., Chen, Y., & Liu, L. (2022). Multi-precision traffic speed predictions via modified sequence to sequence model and spatial dependency evaluation method. *Applied Soft Computing*, *130*, 109700.

Mohammadian, S., Zheng, Z., Haque, M. M., & Bhaskar, A. (2021). Performance of continuum models for realworld traffic flows: Comprehensive benchmarking. *Transportation Research Part B: Methodological*, *147*, 132–167.

Munoz, J. C., & Daganzo, C. F. (2002). The bottleneck mechanism of a freeway diverge. *Transportation Research Part A: Policy and Practice*, *36*(6), 483–505.

Ngoduy, D. (2021). Noise-induced instability of a class of stochastic higher order continuum traffic models. *Transportation Research Part B: Methodological*, *150*, 260–278.

Peng, C., & Xu, C. (2023). A coordinated ramp metering framework based on heterogeneous causal inference. *Computer-Aided Civil and Infrastructure Engineering*, *38*(10), 1365–1380.

Perretti, C. T., Sugihara, G., & Munch, S. B. (2013). Nonparametric forecasting outperforms parametric methods for a simulated multispecies system. *Ecology*, *94*(4), 794–800.

Qin, Y., Wang, H., & Ni, D. (2021). Lighthill-Whitham-Richards model for traffic flow mixed with cooperative adaptive cruise control vehicles. *Transportation Science*, *55*(4), 883–907.

Richards, P. I. (1956). Shock waves on the highway. *Operations research*, *4*(1), 42–51.

Runge, J. (2018). Causal network reconstruction from time series: From theoretical assumptions to practical estimation. *Chaos*, *28*(7), 075310.

Ryu, U., Wang, J., Pak, U., Kwak, S., Ri, K., Jang, J., & Sok, K. (2022). A clustering based traffic flow prediction method with dynamic spatiotemporal correlation analysis. *Transportation*, *49*(3), 951–988.

Saeedmanesh, M., & Geroliminis, N. (2016). Clustering of heterogeneous networks with directional flows based on "snake" similarities. *Transportation research part B: Methodological*, *91*, 250–269.

Shi, H., Zhou, Y., Wang, X., Fu, S., Gong, S., & Ran, B. (2022). A deep reinforcement learning-based distributed connected automated vehicle control under communication failure. *Computer-Aided Civil and Infrastructure Engineering*, *37*(15), 2033–2051.

Spiliopoulou, A., Kontorinaki, M., Papageorgiou, M., & Kopelias, P. (2014). Macroscopic traffic flow model validation at congested freeway off-ramp areas. *Transportation Research Part C: Emerging Technologies*, *41*, 18–29.

Sugihara, G., May, R., Ye, H., Hsieh, C.-H., Deyle, E., Fogarty, M., & Munch, S. (2012). Detecting causality in complex ecosystems. *Science*, *338*(6106), 496–500.

Takens, F. (1981). Detecting strange attractors in turbulence. In D. Rand & L. S. Young (Eds.), *Dynamical systems and turbulence, Warwick 1980. Lecture notes in mathematics*, Vol: 898, pp. 366–381. Springer, Berlin.

Uzal, L. C., Grinblat, G. L., & Verdes, P. F. (2011). Optimal reconstruction of dynamical systems: A noise amplification approach. *Physical Review E*, *84*(1), 016223.

Vlahogianni, E. I., Karlaftis, M. G., & Golias, J. C. (2008). Temporal evolution of short-term urban traffic flow: A nonlinear dynamics approach. *Computer-Aided Civil and Infrastructure Engineering*, *23*(7), 536–548.

Wang, J.-Y., Kuo, T.-C., & Hsieh, C.-H. (2020). Causal effects of population dynamics and environmental changes on spatial variability of marine fishes. *Nature Communications*, *11*(1), 1–10.

Wu, Y., Tan, H., Qin, L., & Ran, B. (2020). Differential variable speed limits control for freeway recurrent bottlenecks via deep actor-critic algorithm. *Transportation Research Part C: Emerging Technologies*, *117*, 102649.

Yang, Y., Heppenstall, A., Turner, A., & Comber, A. (2019). A spatiotemporal and graph-based analysis of dockless bike sharing patterns to understand urban flows over the last mile. *Computers, Environment and Urban Systems*, *77*, 101361.

Ye, H., Beamish, R. J., Glaser, S. M., Grant, S., Hsieh, C. H., Richards, L. J., Schnute, J. T., & Sugihara, G. (2015). Equation-free mechanistic ecosystem forecasting using empirical dynamic modeling. *Proceedings of the National Academy of Sciences of the United States of America*, *112*(13), E1569–E1576.

Ye, H., Deyle, E. R., Gilarranz, L. J., & Sugihara, G. (2015). Distinguishing time-delayed causal interactions using convergent cross mapping. *Scientific Reports*, *5*(1), 1–9.

Zhang, K., Zheng, L., Liu, Z., & Jia, N. (2020). A deep learning based multitask model for network-wide traffic speed prediction. *Neurocomputing*, *396*, 438–450.

Zhang, Z., Guo, M., Fu, D., Mo, L., & Zhang, S. (2022). Traffic signal optimization for partially observable traffic system and low penetration rate of connected vehicles. *Computer-Aided Civil and Infrastructure Engineering*, *37*(15), 2070–2092.

Zhou, A., Peeta, S., & Wang, J. (2023). Cooperative control of a platoon of connected autonomous vehicles and unconnected human-driven vehicles. *Computer-Aided Civil and Infrastructure Engineering*, *38*(18), 2513–2536.

Zhou, X. S., Cheng, Q., Wu, X., Li, P., Belezamo, B., Lu, J., & Abbasi, M. (2022). A meso-to-macro cross-resolution performance approach for connecting polynomial arrival queue model to volume-delay function with inflow demand-to-capacity ratio. *Multimodal Transportation*, *1*(2), 100017.

Zou, X., Chung, E., Zhou, Y., Long, M., & Lam, W. H. (2024). A feature extraction and deep learning approach for network traffic volume prediction considering detector reliability. *Computer-Aided Civil and Infrastructure Engineering*, *39*(1), 102–119.

How to cite this article: Mao, J., Huang, H., Gu, Y., Lu, W., Tang, T., & Ding, F. (2025). A convergent cross-mapping approach for unveiling congestion spatial causality in urban traffic networks. *Computer-Aided Civil and Infrastructure Engineering*, *40*, 301–322. https://doi.org/10.1111/mice.13334

APPENDIX A

A simulation-based experiment using SUMO (i.e., simulation of urban mobility), an open-source microscopic traffic simulation package, evaluates the performance of three methods within a more deterministic network system featuring known traffic inputs and vehicle routes. This network comprises eight nodes that are connected by one lane road as depicted in Figure A1. Inflow enters the network at Node 1, with the volume set to a high value (Q) to trigger congestion. Vehicle routes and their respective vol-

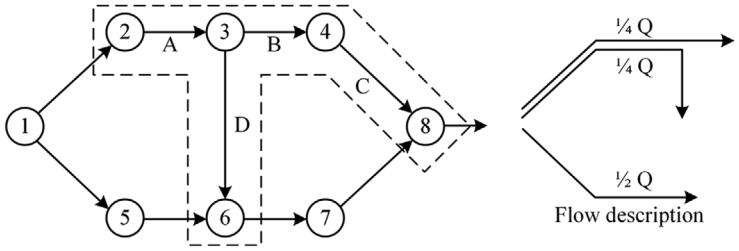

(a) Network structure and traffic inflow description

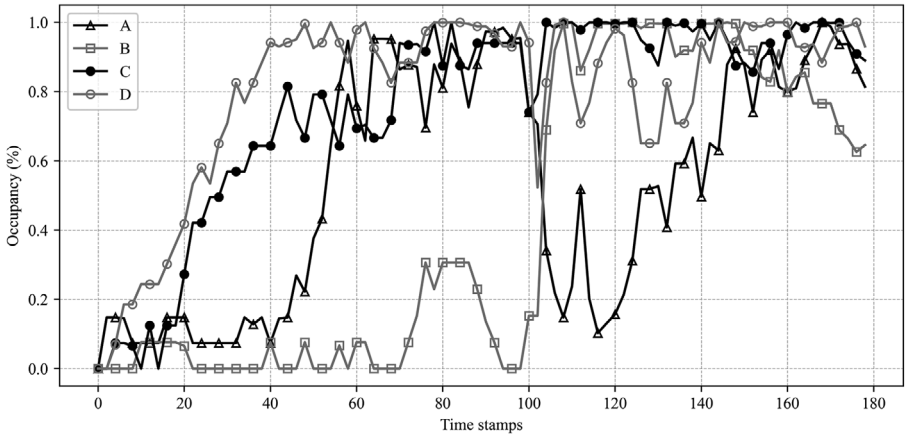

(b) Occupancy of the four selected road sections

FIGURE A1 Illustration of simulation experiment.

TABLE A1 Comparison results in simulation scenario.

Method	Affected road	A	B	C	D
Spatial correlation	A	–	**0.724**	0.415	0.628
	B	**0.724**	–	0.540	0.495
	C	0.415	**0.540**	–	0.245
	D	**0.628**	0.495	0.245	–
Granger causality	A	–	–	4.711	**16.497**
	B	–	–	**16.717**	8.778
	C	**12.068**	3.935	–	7.744
	D	–	–	**5.490**	–
T-CCM	A	–	**0.484**	0.104	0.471
	B	**0.532**	–	0.413	0.323
	C	0.137	**0.332**	–	–
	D	**0.619**	0.366	–	–

Abbreviation: T-CCM, traffic-convergent-cross-mapping.

umes are fixed as illustrated in Figure A1a. Furthermore, vehicles yield to oncoming traffic when turning left, making Nodes 6 and 8 bottlenecks. Hence, road sections A, B, C, and D (outlined with a dotted frame) are selected as the study area.

As in Section 3.3, spatial correlation, Granger causality, and the T-CCM method are evaluated in this simulation scenario. A minor variation is that the occupancy of road sections A, B, C, and D serves as the time-series input as illustrated in Figure A1b. Embedding dimension and time delay are both set to 3. Experimental results are presented in Table A1.

From Table A1, a drawback of spatial correlation is that the detected correlation is symmetrical, and it also incorrectly identifies a dependency between C and D. For Granger causality, its performance is better than the tests

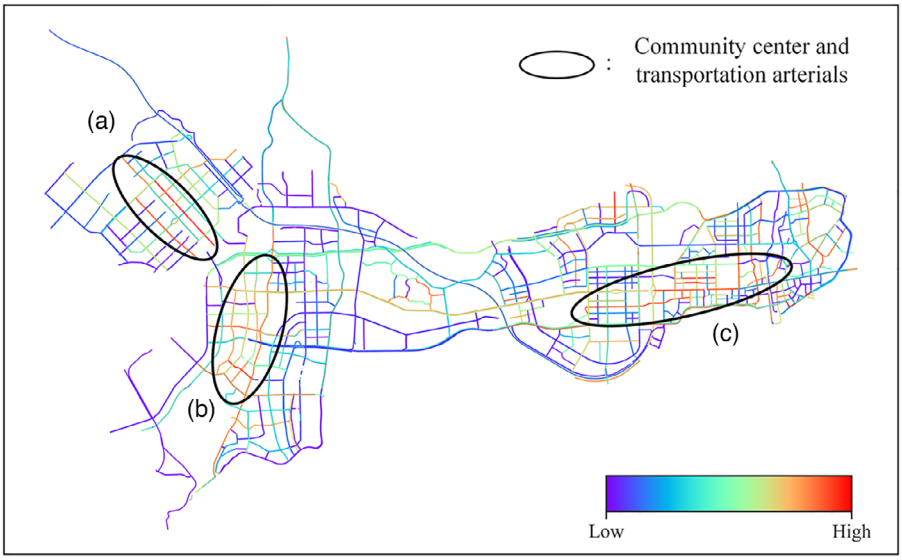

FIGURE A2 Illustration of causality correlation strength in SZ. SZ, Shenzhen.

on actual networks in Section 3.3, yet it still has omissions (no causal relationship between A and B, A and D) and errors (a causal relationship exists between C and D). In comparison, the T-CCM method can accurately determine causal relationships between road sections.

APPENDIX B

This appendix utilizes 2 months of real-world traffic speed data (March and April 2018) from major roads across approximately 200 km^2 in Shenzhen (abbreviated as "SZ"), aiming to identify key influencers within the urban traffic network and illustrate the potential practical value of causality analysis in traffic management.

Similar to Section 3.4, the causality relationships between roads are quantified as degree values, indicating each road's influence on others. These values are represented on a color spectrum ranging from blue (low influence) to red (high influence). The analysis results, depicted in Figure A2, highlight roads with high causality correlation strength primarily located in the community center and along major transportation arterials. These roads are marked with black circles for easy identification.

Roads identified with high causality influence are critical for strategic interventions. By understanding how traffic conditions on one road influence another, traffic management can proactively adjust route guidance and signal timings to alleviate potential bottlenecks. To give a simple example, if roads in area C in Figure A2 significantly affect traffic flow on others, adjustments in signal timings in area C during peak traffic can preemptively reduce congestion. Such targeted actions enhance traffic efficiency and urban network resilience by proactively managing potential congestion points.